

The use of Cauchy-type singular integrals over neighboring intervals to compute induced slip in displaced faults

Meulenbroek, Bernard; Jansen, Jan-Dirk

DOI

[10.1016/j.ijsolstr.2024.112922](https://doi.org/10.1016/j.ijsolstr.2024.112922)

Publication date

2024

Document Version

Final published version

Published in

International Journal of Solids and Structures

Citation (APA)

Meulenbroek, B., & Jansen, J.-D. (2024). The use of Cauchy-type singular integrals over neighboring intervals to compute induced slip in displaced faults. *International Journal of Solids and Structures*, 300, Article 112922. <https://doi.org/10.1016/j.ijsolstr.2024.112922>

Important note

To cite this publication, please use the final published version (if applicable). Please check the document version above.

Copyright

Other than for strictly personal use, it is not permitted to download, forward or distribute the text or part of it, without the consent of the author(s) and/or copyright holder(s), unless the work is under an open content license such as Creative Commons.

Takedown policy

Please contact us and provide details if you believe this document breaches copyrights. We will remove access to the work immediately and investigate your claim.



The use of Cauchy-type singular integrals over neighboring intervals to compute induced slip in displaced faults

Bernard Meulenbroek^a, Jan-Dirk Jansen^{b,*}

^a Delft Institute of Applied Mathematics, Delft University of Technology (TU Delft), The Netherlands

^b Department of Geoscience and Engineering, TU Delft, The Netherlands

ARTICLE INFO

Keywords:

Cauchy singular integral
Inverse solution
Semi-analytical
Gauss–Chebyshev quadrature
Induced seismicity
Displaced fault
Fault slip
Collinear cracks
Coupled solution
Interaction

ABSTRACT

We present expressions to compute the inverse of a Cauchy-type singular integral equation representing the relation between a double-peaked Coulomb stress in a fault or fracture and the resulting slip gradient in two distinct collinear slip patches. In particular we consider a situation where the patches are close enough to account for the influence of the slip gradient in one patch on the slip-induced shear stress in the other patch and vice versa. This situation can occur during depletion-induced or injection-induced fault slip in subsurface reservoirs for, e.g., natural gas production, hydrogen or CO₂ storage, or geothermal operations. The theory for a single slip patch is well-developed but the situation is less clear for a configuration with two patches although the monographs of Muskhelishvili (1953) and Weertman (1996) provide earlier results. We show that the general inverse solution for the coupled two-patch problem requires six auxiliary conditions to ensure six physical requirements: boundedness of the slip gradient at the four end points of the slip patches and vanishing of the integrals of the slip gradient over the patches. Mathematically, the presence of two additional conditions, as compared to earlier formulations, corresponds to two undetermined coefficients in the general solution of the governing integral equation. Numerical simulation confirms that at least one of these is always non-zero in the coupled situation. For a coupled double-patch case with a symmetric pre-slip Coulomb stress pattern, the general inverse solution requires three auxiliary conditions. Moreover the conditions for the asymmetric case may be reduced to a set of four again, but these are different from the sets of four obtained earlier by Muskhelishvili (1953) and Weertman (1996). We illustrate the theory with a numerical example in which the evaluation of the Cauchy integrals is performed with a modified version of augmented Gauss–Chebyshev quadrature that relies on analytical inversion.

1. Introduction

1.1. Motivation

We address the computation of poroelastic stresses and the resulting fault slip caused by injection or production of fluids into/from deep subsurface reservoirs; i.e., fluid-filled poro-elastic inclusions inside fluid-tight elastic surroundings (Segall, 1985, 1989; Suckale, 2009; Elsworth et al., 2016; Foulger et al., 2018; Muntendam-Bos et al., 2022). In particular we aim to better understand the effects of the double-peaked shear stress pattern that occurs when these reservoirs contain displaced faults, i.e. faults with a non-zero offset. The effect of fault offset on induced fault slip seems to have been first addressed in relation to the depletion of hydrocarbon reservoirs, and early numerical studies were made by Roest and Kuilman (1994) and Roest and Mulders (2000) and Mulders (2003). More recent numerical studies

were performed by Van den Bogert (2015, 2018), Buijze et al. (2017, 2019), Van Wees et al. (2017, 2019) and Hergert et al. (2022) who all demonstrated the development of two shear stress peaks, resulting in two aseismic collinear slip patches that grow with increasing depletion until they either merge aseismically or become unstable resulting in a seismic event. The presence of singularities resulting in near-infinite stress peaks and the possibility of unstable fault slip complicates the numerical treatment of the problem and warrants the use of (semi-) analytical techniques to clarify the underlying physics. Such a semi-analytical treatment was reported by Jansen and Meulenbroek (2022) but the formulation of the coupling effect of neighboring slip patches, and thus the understanding of the phenomenon, were incomplete.

1.2. Configuration

We consider a two-dimensional plane-strain model of a subsurface reservoir; see Fig. 1. We assume the reservoir to be either of finite width

* Corresponding author.

E-mail address: j.d.jansen@tudelft.nl (J.-D. Jansen).

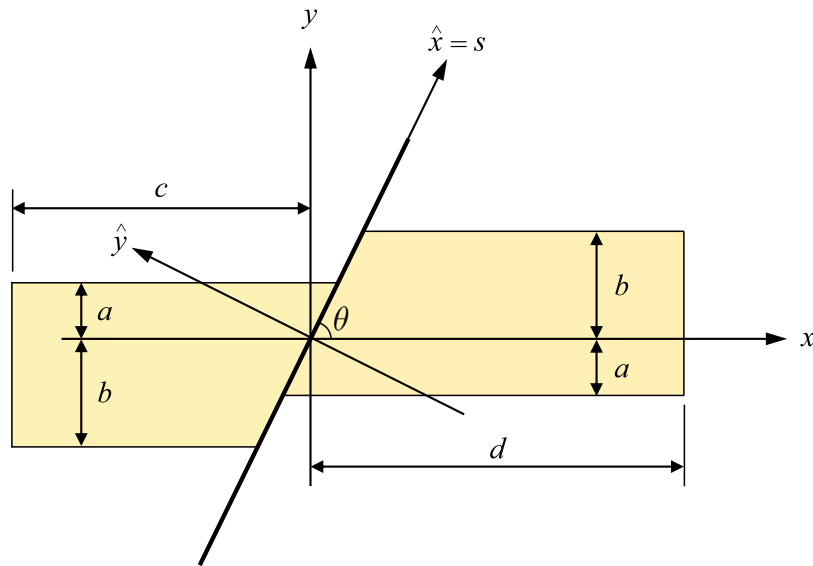


Fig. 1. Reservoir with a displaced fault (Jansen et al., 2019).

or infinitely wide and of height $h = a + b$, intersected by a displaced non-sealing zero-width fault with an offset (also known as fault throw) of magnitude $t_f = b - a$ and a dip angle θ . From the studies listed above that addressed the effect of fault offset in detail it follows that depletion typically results in the development of two slip patches starting from the ‘internal’ reservoir-fault corners at $y = \pm a$; see Fig. 2 which displays results for an example with parameter values given in Table 1. Continuing depletion will usually result in a gradual aseismic growth of the two slip patches until one of them (or occasionally both) becomes unstable and generates a seismic event which then also leads to merging of the patches. In another scenario, which seems to be less frequently occurring, the slip patches merge aseismically (Van den Bogert, 2018).

1.3. Stress peaks

The presence of sharp ‘internal’ and ‘external’ reservoir-fault corners in the reservoir model displayed in Fig. 1 results in positive-valued peaks in the pre-slip Coulomb stress at $y = \pm a$ and negative-valued peaks at $y = \pm b$, see Fig. 2. The physical nature of these peaks stems from the increase in compressive stresses in the grains of the reservoir rock caused by a decrease in reservoir pore pressure, and thus a corresponding vertical compaction. In those segments of the fault where reservoir rock juxtaposes non-reservoir rock, this vertical compaction is restricted by the stiffness of the adjacent non-reservoir rock, which results in severe stress concentrations at the reservoir-fault corners. Appendix A gives an example of this effect and provides closed-form analytical expressions to compute the magnitude of the corresponding stress field.

The stress peaks are, mathematically, of infinite magnitude. In reality, physical effects such as more rounded corners, a finite fault width and pore pressure diffusion between the reservoir and the surrounding rock will somewhat smoothen the stress profile. However, peaks in the pre-slip Coulomb stress profile remain a typical characteristic of displaced faults that experience depletion or injection where it should be noted that, as opposed to the peak configuration during depletion, injection results in positive peaks at the external corners and negative peaks at the internal ones (Jansen et al., 2019). Also, for increasing depletion the ‘internal’ patches will grow further inward with the negative stress peaks at the external corners blocking progression of the slip towards the overburden or underburden. Opposed, during injection the external patches will grow outward, into the overburden and

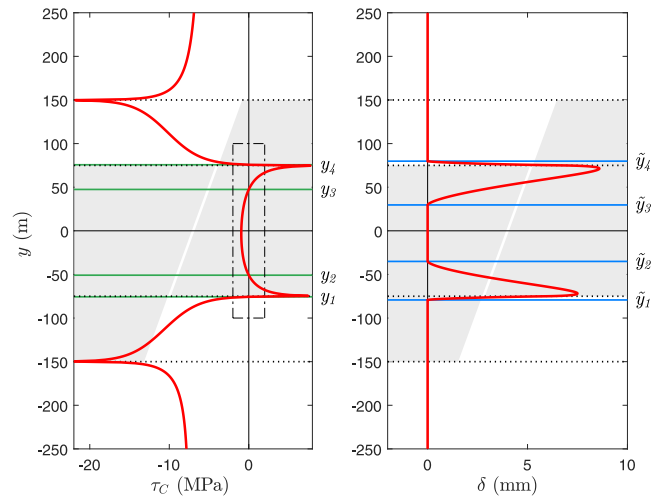


Fig. 2. Pre-slip Coulomb stress and slip for the example with properties listed in Table 1. Left: pre-slip Coulomb stress $\tau_C = \tau - \tau_{si}$. Right: fault slip δ . The green horizontal lines at $y = -76, -51, 47$ and 76 m in the left figure correspond to the zeros y_i of the pre-slip Coulomb stress. The blue horizontal lines at $y = -80, -33, 29$ and 80 m in the right figure correspond to the slip patch boundaries \tilde{y}_i . The horizontal black dotted lines in both figures represent the four coordinate values $y = -a, -b, b$ and a which correspond to the top and bottom of the reservoir blocks, indicated in gray, at each side of the fault. The dash-dotted rectangle in the left figure corresponds to the detailed views in Figs. 4 and 5.

underburden while also the increased reservoir pressure is more likely to propagate outward through the fault causing a further tendency of outward slip propagation.

1.4. Coupling and multiple integration intervals

The two slip patches in a fault are often located far enough from each other to neglect the effect of slip in one patch on the slip in the other one. E.g., in the example with slip-weakening friction considered in Jansen and Meulenbroek (2022) coupling became only relevant for scaled fault offsets t_f/h larger than about 0.7. Also, in case of injection-induced seismicity the slip patches will grow outward, instead of inward like in depletion-induced situations, and coupling will usually be irrelevant. In those cases it is computationally more efficient to

consider the stresses and slip in each of the patches in isolation. However, coupling significantly changes the slip patch growth when the patches approach each other. In Jansen and Meulenbroek (2022) an attempt was made to address the coupling effect with an iterative procedure by alternately considering the effect of fault slip in one patch on the stresses in the other patch and vice versa. However this approach was not computationally efficient while also convergence of the iterative procedure cannot be guaranteed.

Here we present a more rigorous coupling approach based on the theory for Cauchy singular integrals over multiple intervals. Although this theory was already developed by Muskhelishvili in the 1940's, applications to multiple intervals are scarce and appear to be limited to a few publications; see, e.g., Muskhelishvili (1953), Lewin (1968) and Weertman (1996). In particular the book by Weertman (1996) is relevant because it addresses fracture mechanics and describes how the multiple-interval formulation of Muskhelishvili can be used compute the stresses and slip in multiple neighboring cracks. Unfortunately, neither the original formulation by Muskhelishvili (1953) nor the theory as worked out by Weertman (1996) appear to be capable to correctly describe the interaction effects between slip patches in induced fault slip. In the remainder of this paper we will present a solution to overcome this shortcoming.

1.5. Organization of the paper

Section 2 briefly describes the geomechanical background of the problem, and provides the Cauchy-type singular integral equation that governs the slip gradient in two neighboring slip patches. Section 3 describes how to obtain an analytical inverse of the governing Cauchy equation that results in a physically realistic configuration of slip patches, and provides the necessary auxiliary conditions. Section 4 briefly discusses how to numerically compute the integrals that occur in the inverse solution, and Section 5 provides a numerical example. Section 6 shows how a symmetric load pattern leads to a reduced set of auxiliary conditions. The last two sections provide a discussion and a concluding summary. Three Appendices provide further information about the geomechanical formulation of the problem, the derivation of the necessary auxiliary conditions for a consistent inverse solution, and the numerical integration procedure.

2. Singular integral equations for fault slip

2.1. Pre-slip coulomb stresses

Closed-form analytical expressions for depletion-induced stresses in 2D displaced faults were derived by various authors; see, e.g., Jansen et al. (2019), Lehner (2019) and Wu et al. (2021). Appendix A lists the expressions reported in Jansen and Meulenbroek (2022) for a uniform quasi-steady-state pressure field, and we refer to Cornelissen et al. (2024) for a recent overview of similar (semi-)analytical methods that can cope with non-uniform pressures and 3D configurations. Moreover, depletion-induced stresses may be computed with the aid of numerical techniques such as finite element, finite volume or (spectral) boundary element methods. All these techniques can be used to compute the pre-slip Coulomb stress in a fault, defined as

$$\begin{aligned} \tau_C &= \tau - \tau_{sl} \\ &= \tau - (\kappa - \mu\sigma'), \end{aligned} \quad (1)$$

where τ is the shear stress, τ_{sl} the slip threshold, σ' the effective normal stress, κ cohesion and μ the friction coefficient; see also Appendix A. Note that we use the solid mechanics sign convention, in which positive normal stresses correspond to tension. The effective normal stress is then defined as

$$\sigma' = \sigma + \beta p, \quad (2)$$

Table 1

Reservoir properties and fault geometry (Jansen and Meulenbroek, 2022).

Symbol	Property	Value	SI units
a	See Fig. 1	75	m
b	"	150	m
c	"	∞	m
d	"	∞	m
D_0	Depth at reservoir center ($y = 0$)	3500	m
g	Acceleration of gravity	9.81	m/s ²
G	Shear modulus	6500	MPa
K^0	Ratio of initial effective horizontal to vertical stresses	0.5	-
Δp	Incremental reservoir pressure	-25	MPa
p_0^0	Initial reservoir pressure at reservoir center	35	MPa
α	Biot coefficient	0.9	-
β	Effective stress coefficient for fault friction	0.9	-
θ	Dip angle	70	deg.
κ	Cohesion	0	MPa
μ_{st}	Static friction coefficient	0.52	-
ν	Poisson's coefficient	0.15	-
ρ_f	Fluid density	1020	kg/m ³
ρ_s	Solid density	2650	kg/m ³
ϕ	Porosity	0.15	-

Note: the initial vertical stress, initial pressure and initial effective normal stress have been computed as: $\sigma_{yy}^0(y) = [(1 - \phi)\rho_s + \phi\rho_f]g(y - D_0)$, where $\sigma_{yy}^0 < 0$, $p^0(y) = p_0^0 - \rho_f g y$, $\sigma^{00}(y) = \sigma^0(y) + \beta p^0(y)$. (Valid for reservoir, overburden and underburden.)

where σ is the normal stress, β an effective stress factor (typically somewhat smaller than or equal to one) and p the reservoir pressure, i.e. the pore pressure in the reservoir rock. The stresses and the pressure are to be interpreted as *combined* quantities in the sense that they are the sum of *initial* components (indicated with a superscript zero) and *incremental* components (indicated with a prefix Δ):

$$\tau = \tau^0 + \Delta\tau, \quad (3)$$

$$\sigma = \sigma^0 + \Delta\sigma, \quad (4)$$

$$p = p^0 + \Delta p. \quad (5)$$

The initial quantities depend on the burial depth of the reservoir and the regional geological stress regime and may be considered constants. The incremental quantities result from human-induced activities where induced pressures subsequently lead to induced stresses, with positive values of Δp corresponding to fluid injection and negative values to depletion.

For a deep subsurface situation, as considered in our paper, combined normal stresses are always compressive and therefore negative-valued. Also, combined normal and shear stresses are typically a function of position s along the fault and of time, while the friction coefficient may be a function of position, time, temperature, slip, slip rate and/or additional state variables that represent internal mechanisms influencing the friction properties (Ohnaka, 2013; Scholz, 2019). Here we will only consider the simplest possible formulation: constant friction, with a static friction coefficient μ_{st} and no cohesion. Moreover, we will restrict our analysis to very slow, i.e. quasi steady-state, changes in the incremental reservoir pressure Δp such that the stresses are only position-dependent.

Zeros of the pre-slip Coulomb stress, i.e. intersections of the shear stress with the slip threshold, can be obtained by solving iteratively for y from the implicit equation

$$\tau(y) = \tau_{sl}(y), \quad (6)$$

where we use the vertical coordinate $y = s \sin(\theta)$ as independent variable rather than the along-fault coordinate s . For the slip-induced stresses in a displaced fault this results in four values $\{y_1, y_2, y_3, y_4\}$, where

$$-b < y_1 < -a < y_2 < y_3 < a < y_4 < b, \quad (7)$$

as long as the slip patches have not merged, and two relevant values $\{y_1, y_4\}$, where

$$-b < y_1 < -a < 0 < a < y_4 < b, \quad (8)$$

thereafter. In Fig. 2 (left) two zones with positive pre-slip Coulomb stress values are visible, and the corresponding zeros $y_i, i = 1, \dots, 4$, have been indicated with horizontal green lines.

2.2. Slip-induced stresses

In areas where the pre-slip Coulomb stress is positive, fault slip will occur. However, once slip occurs, the stress field in and around the fault changes. In particular, slip-induced shear stresses in the fault occur, which can be shown to have magnitude (Weertman, 1996; Jansen and Meulenbroek, 2022)

$$\check{\tau}(y) = A \left(\text{PV} \int_{\bar{y}_1}^{\bar{y}_2} \frac{\nabla \delta(\xi)}{\xi - y} d\xi + \text{PV} \int_{\bar{y}_3}^{\bar{y}_4} \frac{\nabla \delta(\xi)}{\xi - y} d\xi \right), \quad (9)$$

where, for plane-strain conditions,

$$A = \frac{G}{2\pi(1-\nu)}, \quad (10)$$

with G representing the shear modulus and ν Poisson's ratio, and

$$\nabla \delta(\xi) = \left. \frac{\partial \delta(y)}{\partial y} \right|_{y=\xi}, \quad (11)$$

with $\delta(y)$ representing the slip and $\nabla \delta(y)$ the slip gradient along the fault. The variables $\bar{y}_i, i = 1, \dots, 4$, in Eq. (9) are horizontal projections on the y axis of the lower and upper slip patch boundaries \bar{s}_i . The prefixes PV in Eq. (9) indicate that either of the integrands may become singular when $\xi = y$. The integral concerned is then a Cauchy-type singular integral, or a Cauchy integral for short, and has to be interpreted in a principal value (PV) sense (Muskhelishvili, 1953; Estrada and Kanwal, 2000). We will not indicate the singularity of integrals in the remainder of this paper, and therefore tacitly assume that they represent a principal value whenever relevant.

The pairs of slip patch boundaries $\{\bar{y}_1, \bar{y}_2\}$ and $\{\bar{y}_3, \bar{y}_4\}$ each span a somewhat larger domain than the corresponding pairs of pre-slip Coulomb stress zeros $\{y_1, y_2\}$ and $\{y_3, y_4\}$. In Fig. 2 (right) the four patch boundaries \bar{y}_i have been indicated with horizontal blue lines which are located just above or below the corresponding values of y_i , indicated with green lines in the left figure. Once slip has occurred, the post-slip Coulomb stress $\check{\tau}_C$ inside the two slip patches will be equal to zero, while outside the patches it will be negative-valued.

Eq. (9) is based on the application of dislocation theory and fracture mechanics to describe fault slip (Bilby and Eshelby, 1968; Rice, 1968, 1980; Weertman, 1996; Segall, 2010). Dislocation theory is defined for elastic media, but may be also applied to poroelastic media because the effects of pore pressure enter the theory of poroelasticity in an additive fashion (Wang, 2000). In our application, moreover, we assume that the elastic properties of the reservoir rock are identical to those of the non-reservoir rock. Other assumptions include the presence of only one, infinitely thin, fault, which is straight such that the two slip patches are collinear.

In dislocation theory, dilation or compaction of the slip plane does not play a role, and slip therefore does not result in a change in normal stresses. In reality, dilation or compaction may play a significant role, especially in situations where direct injection takes place into a permeable-gouge-filled fault in a relatively less permeable reservoir; see, e.g., Heimissson et al. (2022). Also, curvature of the fault may introduce normal stresses. However, we focus on highly permeable reservoirs without direct injection into faults, while we only consider straight faults, and we therefore adhere to the approximation that slip only results in shear stress changes. Moreover, we assume that in areas where slip occurs the post-slip Coulomb stress becomes exactly equal to zero; i.e., slip does not result in an overshoot that would lead to negative post-slip Coulomb stresses in areas where the pre-slip stresses were positive. This latter assumption may be challenged when slip results in a seismic event but is justified for aseismic slip. In any case,

the assumption of zero post-slip Coulomb stress in a slipping patch implies that we should have

$$\check{\tau} = -\tau_C, \quad (12)$$

such that Eq. (9) becomes

$$-\tau_C(y) = A \left(\int_{\bar{y}_1}^{\bar{y}_2} \frac{\nabla \delta(\xi)}{\xi - y} d\xi + \int_{\bar{y}_3}^{\bar{y}_4} \frac{\nabla \delta(\xi)}{\xi - y} d\xi \right), \quad (\bar{y}_1 < y < \bar{y}_2) \vee (\bar{y}_3 < y < \bar{y}_4). \quad (13)$$

If the two slip patches are located far from each other, coupling effects may be neglected and we can use the equation for a single patch:

$$-\tau_C(y) = A \int_{\bar{y}_-}^{\bar{y}_+} \frac{\nabla \delta(\xi)}{\xi - y} d\xi, \quad \bar{y}_- < y < \bar{y}_+, \quad (14)$$

where $(\bar{y}_-, \bar{y}_+) = (\bar{y}_1, \bar{y}_2)$ or $(\bar{y}_-, \bar{y}_+) = (\bar{y}_3, \bar{y}_4)$ depending on whether we consider the bottom patch or the top patch. Eq. (14) also holds after the slip patches have merged in which case we have $(\bar{y}_-, \bar{y}_+) = (\bar{y}_1, \bar{y}_4)$.

2.3. Continuity requirement

For a known pre-slip Coulomb stress distribution τ_C , both the slip gradient $\nabla \delta(y)$ and the patch boundaries \bar{y}_i are unknowns that have to be determined from the inverse of Eq. (13) or (14) and additional conditions. Muskhelishvili (1953) proved that an analytical inversion of singular integral equations can be obtained provided the known function in the integrand is Hölder continuous, which is a stricter form of continuity than regular continuity as applied in mathematical analysis. As discussed in detail by Jansen and Meulenbroek (2022), the closed-form expressions for induced pre-slip Coulomb stresses in a displaced fault contain jump discontinuities at coordinate values $y = \{-b, -a, a, b\}$ in addition to singularities in the form of infinite stress peaks. The jump discontinuities clearly violate the regular and Hölder continuity conditions. An effective way to overcome this difficulty is to regularize the expressions for the shear and normal stresses in the fault, an approach was followed by Jansen and Meulenbroek (2022), and their regularized expressions have been reproduced in Appendix A.5 in Appendix A.

3. Inverse

3.1. General solution

In the monograph by Estrada and Kanwal (2000) it is shown that the inverse of Eq. (13) can be obtained as (see also Appendix B)

$$\nabla \delta(y) = \frac{1}{\pi^2 A \Psi_{\pm}(y)} \left(\int_{\bar{y}_1}^{\bar{y}_2} \frac{-\tau_C(\xi) \Psi_{-}(\xi)}{y - \xi} d\xi + \int_{\bar{y}_3}^{\bar{y}_4} \frac{-\tau_C(\xi) \Psi_{+}(\xi)}{y - \xi} d\xi + C_0 + C_1 y \right), \quad (15)$$

where

$$\Psi_{\pm}(y) = \pm \sqrt{-(y - \bar{y}_1)(y - \bar{y}_2)(y - \bar{y}_3)(y - \bar{y}_4)}, \quad (16)$$

with the plus and minus signs preceding the square root term corresponding to $\bar{y}_3 < y < \bar{y}_4$ and $\bar{y}_1 < y < \bar{y}_2$ respectively. The last two terms at the right-hand side of Eq. (15), with the undetermined coefficients C_0 and C_1 , form the solution of the homogeneous part of Eq. (13), while the two integral terms form the particular solution for $-\tau_C(y)$.

If coupling can be disregarded, each of the two slip patches can be considered in isolation with the inverse solution of Eq. (14) (Estrada and Kanwal, 2000):

$$\nabla \delta(y) = \frac{1}{\pi^2 A \Phi(y)} \left(\int_{\bar{y}_-}^{\bar{y}_+} \frac{-\tau_C(\xi) \Phi(\xi)}{\xi - y} d\xi + C_0 \right), \quad (17)$$

where

$$\Phi(y) = \sqrt{-(y - \bar{y}_-)(y - \bar{y}_+)}. \quad (18)$$

3.2. Conditions for a bounded solution

Both inverse Eqs. (15) and (17) contain singularities at the end points \bar{y}_i of the slip patches because of the presence of the terms $\Psi(y)$ and $\Phi(y)$ in the denominators of the fractions preceding the integral terms, leading to unbounded values for the slip gradient in the end points. However, it is well known that a bounded solution of Eq. (17) can be obtained by rewriting it as

$$\nabla\delta(y) = \frac{\Phi(y)}{\pi^2 A} \int_{\bar{y}_-}^{\bar{y}_+} \frac{-\tau_C(\xi)}{\Phi(\xi)(\xi - y)} d\xi, \quad (19)$$

which is possible provided the following two conditions are fulfilled (Bilby and Eshelby, 1968); see also Appendix B:

$$I_i = \int_{\bar{y}_-}^{\bar{y}_+} \frac{-\tau_C(y) y^i}{\Phi(y)} dy = 0, \quad i = 0, 1. \quad (20)$$

Note that terms $\Phi(\xi)$ and $\Phi(y)$ are now present in the denominators of the integrands in Eqs. (19) and (20) respectively, such that singularities occur at the boundaries of the integration domain. However, it can be shown that (the PVs of) the integrals have finite values. Also note that the constant C_0 that was present in Eq. (17) has disappeared in the transformed Eq. (19). It is shown in Appendix B.2 in Appendix B that the vanishing of C_0 follows from an additional condition to ensure that the slip remains zero at both ends of the slip patch:

$$\int_{\bar{y}_-}^{\bar{y}_+} \nabla\delta(y) dy = 0. \quad (21)$$

While condition (21) thus serves to determine the value of C_0 , the other two conditions (20) can be used to iteratively search for the values of the two end points \bar{y}_- and \bar{y}_+ of each slip patch; see, e.g., Bilby and Eshelby (1968), Mavko (1982), Weertman (1996), Uenishi and Rice (2003) and Segall (2010). Once these points have been found, Eq. (19) can be integrated to obtain the slip gradient $\nabla\delta(y)$. Thereafter, the along-fault slip in each of the slip patches can be determined through another integration according to

$$\delta(y) = \int_{\bar{y}_-}^y \nabla\delta(\xi) d\xi, \quad (22)$$

where we make use of our knowledge that $\delta(\bar{y}_-) = 0$. Both integrations can be performed numerically, or semi-analytically in terms of an expansion in Chebyshev polynomials; see, e.g., Mavko (1982), Uenishi and Rice (2003), Segall (2010) and Jansen and Meulenbroek (2022).

Returning to the coupled inverse Eq. (15), conditions to obtain a bounded solution appear to be less well known. In Appendix B.2 of Appendix B it is shown that Eq. (15) can be rewritten as

$$\nabla\delta(y) = \frac{\Psi_{\pm}(y)}{\pi^2 A} \left(\int_{\bar{y}_1}^{\bar{y}_2} \frac{-\tau_C(\xi)}{\Psi_{-}(\xi)(\xi - y)} d\xi + \int_{\bar{y}_3}^{\bar{y}_4} \frac{-\tau_C(\xi)}{\Psi_{+}(\xi)(\xi - y)} d\xi \right), \quad (23)$$

which is bounded provided six conditions are fulfilled from which it is then possible to solve for the four slip patch boundaries $\bar{y}_i, i = 1, \dots, 4$, and the unknown coefficients C_0 and C_1 . The first four conditions can be expressed as

$$C_0 + (\bar{y}_1 + \bar{y}_2 + \bar{y}_3 + \bar{y}_4)C_1 + I_3 = 0, \quad (24)$$

$$C_1 + I_2 = 0, \quad (25)$$

$$I_1 = 0, \quad (26)$$

$$I_0 = 0. \quad (27)$$

with

$$I_i = \int_{\bar{y}_1}^{\bar{y}_2} \frac{-\tau_C y^i}{\Psi_{-}(y)} dy + \int_{\bar{y}_3}^{\bar{y}_4} \frac{-\tau_C y^i}{\Psi_{+}(y)} dy = 0, \quad i = 0, \dots, 3, \quad (28)$$

while the additional conditions to determine C_0 and C_1 are given by the equalities

$$\int_{\bar{y}_1}^{\bar{y}_2} \nabla\delta(y, C_0, C_1) dy = 0, \quad \int_{\bar{y}_3}^{\bar{y}_4} \nabla\delta(y, C_0, C_1) dy = 0, \quad (29)$$

which ensure vanishing slip at the ends of both slip patches. We note that numerical evaluation reveals that coefficient C_0 always has a non-zero value whereas C_1 vanishes for the examples considered in our study; see also the remarks in Appendix B.

An alternative formulation, which requires only four conditions, is also presented in Appendix B. Although mathematically the two formulations are equivalent, the four-condition formulation is slightly faster than the six-condition version, but it is less robust in the sense that it is more prone to numerical (integration) errors.

In case of continued depletion, the slip patches will grow inward and may eventually merge. Thereafter, the slip gradient is governed by a single-interval equation, identical to Eq. (17) with $\bar{y}_- = \bar{y}_1$ and $\bar{y}_+ = \bar{y}_4$.

3.3. Comparison with earlier formulations

The original treatment of the coupled inversion problem by Muskhelishvili (1953) states that four conditions are sufficient to guarantee boundedness of the inverse expression, if all end points are bounded, and these conditions would then be identical to the ones in Eqs. (24) to (27) but with vanishing C_0 and C_1 . Echoes of this statement can be found in later publications; see, e.g., Pogorzelski (1966). As discussed in detail in Appendix B, these conditions would indeed be sufficient if only the direct inverse of the Cauchy equation would be of physical relevance, i.e., the slip gradient $\nabla\delta$. However, it is primarily the slip δ that is of interest in fault mechanics, and therefore the four conditions of Muskhelishvili (1953) are insufficient for a physically consistent solution in our application. (Weertman, 1996) provides a slightly different set of four conditions of which the first three are similar to those of Muskhelishvili (1953), whereas the fourth one is different; see Appendix B.5 in Appendix B. Both these earlier sets of conditions do lead to bounded solutions for $\nabla\delta$. However, subsequent integration to obtain the slip δ then produces physically unrealistic results, i.e., slip values that are not equal to zero at the slip patch boundaries. This therefore prompted us to derive a more general bounded inverse solution, which was summarized above and is described in detail in Appendix B.

4. Numerical integration

4.1. Chebyshev polynomials

Cauchy integrals and their corresponding inverse expressions can often be manipulated efficiently with the aid of Chebyshev polynomials (Mason and Handscomb, 2003). Applications in aerodynamics, contact mechanics and fracture mechanics involve both (semi-)analytical approaches, and numerical methods that strongly rely on the underlying analytical properties of Chebyshev polynomials; see, e.g., Golberg (1990), Hills et al. (1996) and Viesca and Garagash (2018). In the geophysical domain, direct semi-analytical solutions have been applied to model fault slip by Mavko (1982), Segall (2010), Bruhat and Segall (2017) and Jansen and Meulenbroek (2022), while a closely related numerical approach was used by Uenishi and Rice (2003), Viesca and Rice (2012) and Garagash and Germanovich (2012).

Chebyshev polynomials come in four kinds, but we will only be concerned with two of them: first-kind polynomials $T_n(z)$ and second-kind polynomials $U_n(z)$, where the dimensionless variable $-1 \leq z \leq 1$ indicates the domain of definition and the integer $0 \leq n < \infty$ the order of the polynomial (Mason and Handscomb, 2003). The first-kind polynomials are defined as $T_n(z) = \cos(n\chi)$ with $z = \cos \chi$. Their zeros, known as first-kind Chebyshev points, are projections on the z axis of equally spaced points on the unit circle, resulting in an increasingly dense distribution of the zeros towards the end points of the domain. A similar, but slightly different, set of second-kind Chebyshev points consists of the zeros of the second-kind polynomials $U_n(z)$. The first-kind and second-kind polynomials are closely related, with $\frac{dT_n}{dz} = nU_{n-1}$, and both sets of Chebyshev points look very similar and are increasing

in density towards the end points. Also, both sets can approximate functions on a finite domain very efficiently through expansion in infinite series, using the polynomials' orthogonality properties, with the difference, however, that first-kind polynomials are best suited to approximate functions with end point singularities, whereas the second-kind variety is the best choice to approximate functions with finite end points.

In an earlier publication (Jansen and Meulenbroek, 2022) we used a peculiar property of Chebyshev polynomials, following similar applications by, e.g., Mavko (1982), Uenishi and Rice (2003) and Segall (2010): expansion of a known function in a Cauchy integral in terms of first-kind polynomials allows for a direct inversion of that integral in terms of second-kind polynomials and vice versa (Mason and Handscorn, 2003). This leads to a semi-analytical description of induced stresses in a displaced fault, which is relatively simple to implement as long as coupling between the slip patches can be disregarded. For the coupled problem, a more convenient approach is the use of (augmented) Gauss–Chebyshev quadrature, a numerical integration method that is strongly dependent on the orthogonality properties of the various Chebyshev polynomials and that uses the corresponding Chebyshev points as quadrature points. It was used successfully for crack problems by, e.g., Hills et al. (1996) and Viesca and Garagash (2018), based on earlier work of Erdogan and Gupta (1972) and Erdogan et al. (1973). As noted by Kalandiyaya (1975), an early derivation of this method was already published by Multhopp (1938). In our current paper we follow this approach and also use Gauss–Chebyshev quadrature, although with a modification: rather than numerical (matrix) inversion, as was used in the earlier publications, we employ the analytical inversion approach described above.

4.2. Augmented Gauss-Chebyshev quadrature with analytical inversion

Erdogan and Gupta (1972) proposed an augmented numerical integration method for Cauchy-type singular integrals based on an earlier Gauss–Chebyshev integration scheme for non-singular integrals. The latter makes use of a non-equidistant set of supports consisting of Chebyshev points, and weight functions based on the discrete orthogonality properties of the Chebyshev polynomials. Erdogan and Gupta (1972) introduced a complementary set of points, in between the Chebyshev points, to avoid singularities while evaluating the difference term in the denominator; i.e., the term $(y - \xi)$ in the various Cauchy equations discussed above. They employed a numerical (matrix) inversion approach to solve for the unknown function in the integral, as part of the integration procedure. In our approach we only use the quadrature elements of the original augmented Gauss–Chebyshev scheme, whereas the inversion is performed analytically, prior to integration. As a result, the optimal choice of the kind of Chebyshev polynomials is determined by the nature of the end points of the known function (bounded or unbounded) rather than by the expected nature of the endpoints of the unknown function, as in the original method. In the current application we only require expressions corresponding to first-kind and second-kind polynomials, and we refer to Appendix C for details of the computational scheme and the (spectral) convergence properties of our modified augmented Gauss–Chebyshev approach.

5. Numerical example

Fig. 3 depicts the pre-slip Coulomb stress zeros $y_i, i = 1, \dots, 4$ and slip patch boundaries \tilde{y}_i as a function of depletion $-\Delta p$. As an example of how to read this graph, two green double arrows illustrate the zones where the pre-slip Coulomb stress is positive for a depletion value $\Delta p = -22$ MPa. For increasing depletion, these zones, in between the green curves, grow in size until they merge at around $\Delta p = -29$ MPa. The two red double arrows similarly illustrate the size of the slip patches for $\Delta p = -23$ MPa. The blue curves indicate their growth with increasing depletion if coupling is disregarded, whereas the red curves

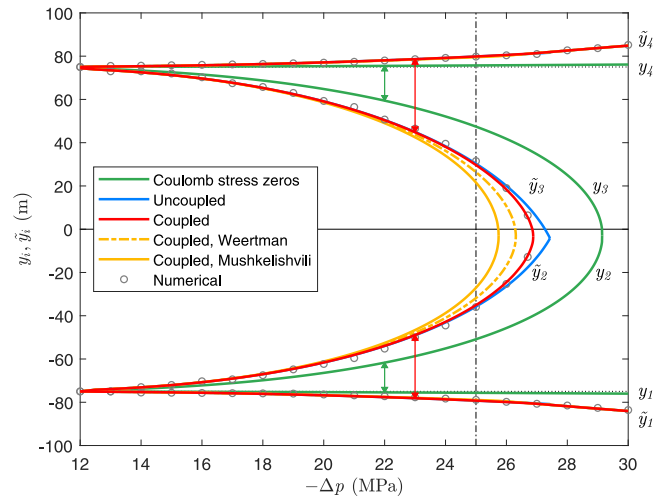


Fig. 3. Pre-slip Coulomb stress zeros $y_i, i = 1, \dots, 4$ and slip patch boundaries \tilde{y}_i as a function of depletion pressure $-\Delta p$. The vertical dash-dotted black line indicates the reference pressure $\Delta p = -25$ MPa which was used to produce the red curves in Figs. 2, 4 and 5.

indicate the correct result with coupling taken into account, resulting in merging just before $\Delta p = -27$ MPa. The orange solid and dash-dotted curves represent the physically unrealistic results obtained by using the formulations of Muskhelishvili (1953) and Weertman (1996). To validate our semi-analytical results, we also performed a numerical simulation with a finite-volume approach (Novikov et al., 2022, 2023). The numerical results, which have been displayed with gray circular markers, confirm our findings. Note that all curves, and the marker set, are slightly asymmetric with respect to the line $y = 0$ because the initial stresses and initial pressure increase with depth.

Fig. 4 displays the pre-slip Coulomb stress, slip gradient and slip for increasing depletion. In the right figure, two slip patches are visible for depletion values of -24 up to -26 MPa, whereas for higher depletion values (-27 and -28 MPa) a single merged patch can be distinguished.

Fig. 5 displays the same red curves as in Fig. 4 but with additional information. The left figure illustrates the relationship between the pre-slip and post-slip Coulomb stresses and the slip-induced shear stress. The post-slip Coulomb stress $\tilde{\tau}_C$ in a fault with slipping patches is obtained as

$$\tilde{\tau}_C = \tau_C + \tilde{\tau}, \quad (30)$$

where we recall that τ_C is the pre-slip Coulomb stress and $\tilde{\tau}$ the slip-induced shear stress. Inside the slip patches, this post-slip Coulomb stress is equal to zero because in those areas the slip-induced stress $\tilde{\tau}$ just compensates the pre-slip stress τ_C ; see Eq. (12). Outside of the slip patches, $\tilde{\tau}_C$ must be smaller than zero because otherwise slip would have occurred. Numerical values of $\tilde{\tau}$ at any point along the y axis can be computed with aid of Eq. (9) once the values for the slip gradient and the slip patch boundaries are known.

The middle and left figures illustrate that the Muskhelishvili (1953) and Weertman (1996) formulations lead to inconsistent results: the slip gradients in the middle figure vanish at the end points of the slip patches; however, the corresponding slip values in the right figure display non-zero end points, a results that is physically incorrect.

6. Symmetry

As can be seen in Figs. 2 to 5, the Coulomb stress pattern and the resulting fault slip pattern are almost symmetric around the line $y = 0$. Logically, the slip gradient pattern is almost anti-symmetric. The reason for these small asymmetries is the increase in the initial Coulomb stress

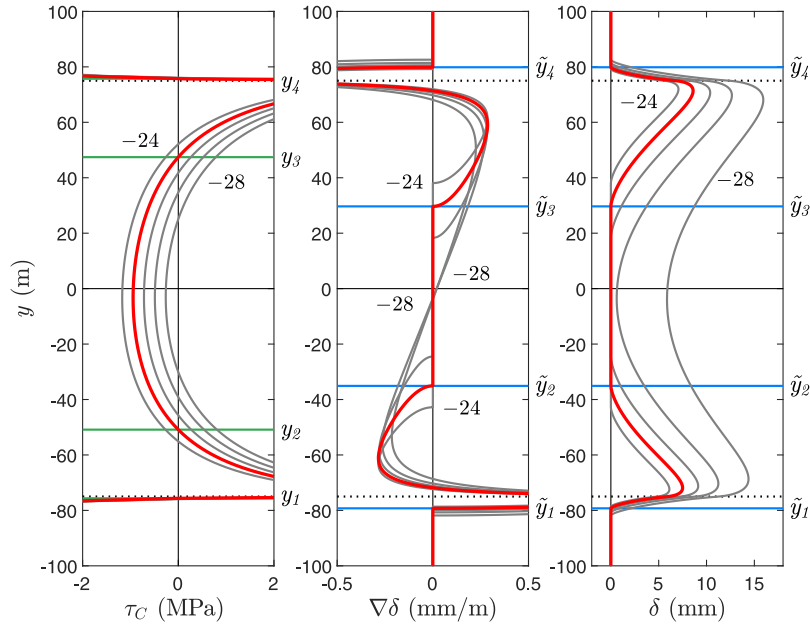


Fig. 4. Pre-slip Coulomb stress, slip gradient and slip for multiple depletion values (detailed view). Left: pre-slip Coulomb stress τ_C . Middle: slip gradient $\nabla\delta$. Right: slip δ . In all three figures, the red curves correspond to $\Delta p = -25$ MPa, while the gray curves correspond to $\Delta p = -24, -26, -27$ and -28 MPa. For the key to solid green, solid blue and dotted black horizontal lines: see Fig. 2.

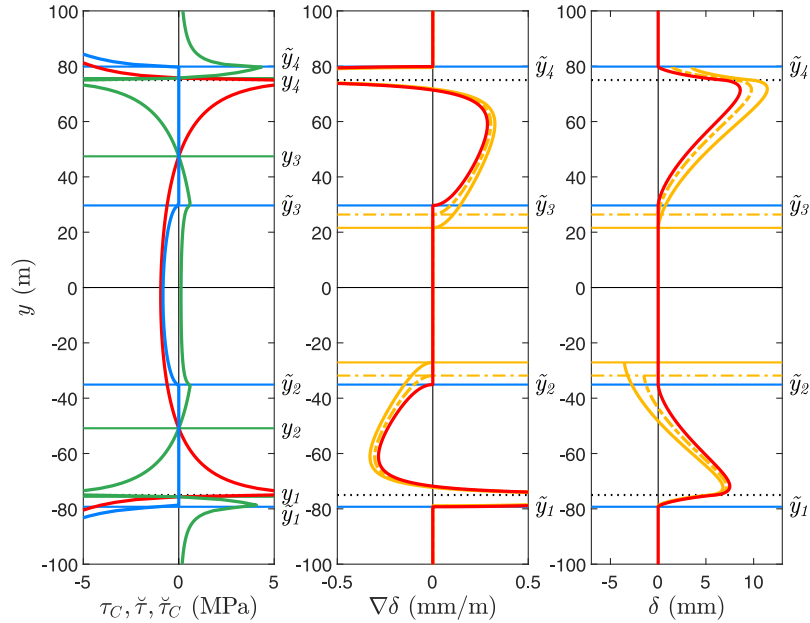


Fig. 5. Pre-slip Coulomb stress, slip gradient and slip for reference pressure $\Delta p = -25$ MPa (detailed view). Left: pre-slip Coulomb stress τ_C (red), slip-induced shear stress $\tilde{\tau}$ (green) and post-slip Coulomb stress $\tilde{\tau}_C$ (blue). Middle: slip gradient $\nabla\delta$. Right: slip δ . In all three figures, the red curves are identical to those in Fig. 4. In the middle and right figures, the solid orange and dash-dotted orange curves represent the [Muskhelishvili \(1953\)](#) and [Weertman \(1996\)](#) results respectively. Solid and dash-dotted horizontal orange lines indicate the corresponding slip patch boundaries. For the key to solid green, solid blue and dotted black horizontal lines: see Fig. 2.

and the initial pressure with depth. If the reservoir height is much smaller than the average reservoir depth below surface, the pressure gradient and initial stress gradient over the height of the reservoir are small compared to their average values in the reservoir. In that case we can use the approximations $y_1 = -y_4$ and $y_2 = -y_3$, and [Appendix B.6](#) describes the derivation of the resulting simplified expressions for the slip gradient. For the symmetric double-patch configuration this leads to

$$\nabla\delta(y) = \frac{\tilde{\Psi}_{\pm}(y)}{\pi^2 A} \int_{\tilde{y}_3}^{\tilde{y}_4} \frac{-2\xi\tau_C(\xi)}{\tilde{\Psi}_{\pm}(\xi)(y^2 - \xi^2)} d\xi, \quad (31)$$

where

$$\tilde{\Psi}_{\pm}(y) = \pm\sqrt{(y^2 - \tilde{y}_3^2)(\tilde{y}_4^2 - y^2)}, \quad (32)$$

with the plus and minus signs preceding the square root term corresponding to $y > 0$ and $y < 0$ respectively. Three conditions, instead of six, are now sufficient to determine \tilde{y}_3 and \tilde{y}_4 and the unknown coefficient C_0 . They can be expressed as

$$I_1 = 0, \quad I_3 + C_0 = 0, \quad \int_{\tilde{y}_3}^{\tilde{y}_4} \nabla\delta(y, C_0) dy = 0, \quad (33)$$

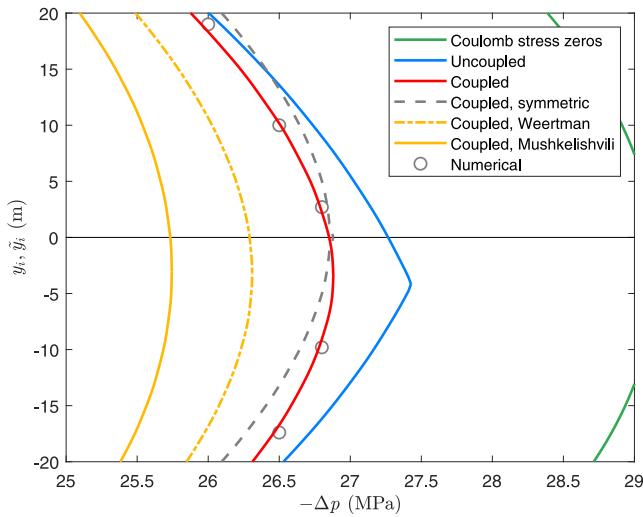


Fig. 6. Zoomed-in version of Fig. 3 with an additional dashed gray curve representing the symmetric result.

with

$$I_i = \int_{\bar{y}_3}^{\bar{y}_4} \frac{-2\tau_C(y) y^i}{\tilde{\Psi}_+(y)} dy, \quad i = 1, 3. \quad (34)$$

Just like in the asymmetric situation, an alternative set of conditions, two in this case, can also be derived to determine \bar{y}_3 and \bar{y}_4 without the need to compute C_0 but at the price of a somewhat reduced numerical robustness.

For the symmetric single-patch case, as occurs after merging, we find

$$\nabla \delta(y) = \frac{2y\tilde{\Phi}(y)}{\pi^2 A} \int_0^{\bar{y}_4} \frac{-\tau_C(\xi)}{\tilde{\Phi}(\xi)(y^2 - \xi^2)} d\xi, \quad (35)$$

where

$$\tilde{\Phi}(y) = \sqrt{\bar{y}_4^2 - y^2}, \quad (36)$$

with a single condition to determine \bar{y}_4 :

$$I_0 = \int_0^{\bar{y}_4} \frac{-2\tau_C(y)}{\tilde{\Phi}(y)} dy = 0. \quad (37)$$

Fig. 6 depicts a zoomed-in version of Fig. 3 with an additional dashed gray curve. It represents the coupled result for a symmetric situation obtained by disregarding the depth-dependence of the initial Coulomb stress and the initial pressure, and using constant values instead, chosen as those at the vertical center of the reservoir (i.e. at $y = 0$).

7. Discussion

We presented a semi-analytical formulation to describe the interaction effects between neighboring slip patches during the development of fault slip in a 2D depletion-induced seismicity setting. The key purpose of our paper was to develop a method to quantify these effects building on the classic theories of singular integral equations and dislocation-based fracture mechanics (Muskhelishvili, 1953; Weertman, 1996). Our approach is restricted to a poroelastic reservoir with uniform properties embedded in an infinite elastic continuum with the same elastic properties as the reservoir. Other assumptions include a perfectly straight and infinitely thin fault with two collinear slip patches without flow along the fault, a simple static friction model, and the absence of multiphase and pressure-transient effects.

In terms of fracture mechanics the fault slip considered in our paper corresponds to a mode-II (in-plane shear) fracture. However, the

same theory is valid for mode-I (extensional) and mode-III (out-of-plane shear) fractures. For the latter, the only change required is to replace the coefficient $A = \frac{G}{2\pi(1-\nu)}$ (valid for modes I and II) by $A = \frac{G}{2\pi}$.

In the example presented in our paper, we modeled a completely conductive fault such that the pore pressures to the left and the right of the fault are identical. However, our approach remains valid for a situation with a non-conductive fault and different pressures at both sides. We note that in the extreme case of zero incremental pressure at one side of the fault and a non-zero value at the other side (i.e. for a bounding fault), there are only two (instead of four) pressure peaks, a positive and a negative one, such that only a single slip patch will develop (Van den Bogert, 2015; Wu et al., 2021; Cornelissen et al., 2024).

A particular feature of induced fault slip in a displaced fault, as considered in our paper, is the occurrence of sharp peaks in the pre-slip Coulomb stress distribution, which mathematically are of infinite magnitude and also show jump-discontinuities. We used a regularization approach to circumvent these issues, resulting in finite and continuous pre-slip Coulomb stresses. However, these stresses still contain sharp peaks such that we require a high number of integration points (typically several hundreds) to resolve them in the augmented Gauss–Chebyshev numerical integration procedure to compute the slip gradient and the slip. An alternative approach would be to split each of the integration intervals in two segments, one below and one above the peak, as long as the patches have not merged, or in three intervals after merging.

A semi-analytical treatment of fault slip in case of slip-weakening friction was performed by Uenishi and Rice (2003). They showed that under slip-weakening conditions, and for a gradually increasing peak-shaped pre-slip Coulomb stress, the fault slip initially occurs a-seismically until the slip patch reaches a critical length, also known as the nucleation length. Beyond this length, equilibrium is no longer possible and seismic slip occurs. Uenishi and Rice (2003) also showed that, mathematically, determining the nucleation length for slip-weakening friction becomes an eigenvalue problem. An extension of this approach, to describe fault slip in a displaced fault with two slip patches, was made by Jansen and Meulenbroek (2022). In that paper, however, the coupling effect between the slip patches could only be taken into account in an approximate, iterative fashion, and only for the simulation of fault slip, but not in the eigenvalue analysis to determine the nucleation length. The theory in the present paper offers a basis to simulate the effect of coupling more rigorously under slip-weakening conditions and also incorporate it in the eigenvalue analysis.

8. Concluding summary

We considered expressions to compute the inverse of a Cauchy-type singular integral equation representing the relation between pre-slip Coulomb stress in a fault or fracture with constant Coulomb friction and the resulting slip gradient. In particular, we derived expressions for a situation where the Coulomb stress distribution displays two neighboring peaks, resulting in slip in two distinct slip patches that are close enough to account for the influence of the slip gradient in one patch on the slip-induced shear stress in the other patch and vice versa.

In our derivation we initially followed the theory of Muskhelishvili (1953) who showed that inversion of the governing Cauchy equation requires auxiliary conditions to ensure boundedness of the slip gradient at the boundaries of the slip patches. The theory for a single slip patch is well-developed and it can be shown that two conditions in the form of integrals over the slip patch, in terms of the pre-slip Coulomb stress and its first moment, are sufficient to guarantee boundedness of the two end point values (Muskhelishvili, 1953; Bilby and Eshelby, 1968; Estrada and Kanwal, 2000). Moreover, in case of a single slip patch these conditions also result in the vanishing of the integral of the slip gradient over the slip patch, which implies that a zero-valued boundary

condition for the slip at one end of the patch leads to a zero value of the slip at the other end, a result that makes physical sense because we require continuity of the slip at both boundaries.

For a two-patch configuration, the situation is less clear. [Muskhelishvili \(1953\)](#) states that four integral conditions are now required to ensure boundedness of the slip gradient at the four slip patch boundaries. We showed that four such conditions are indeed required to ensure boundedness of the slip gradient, and that the conditions given by [Muskhelishvili \(1953\)](#) do lead to that result. However, we also showed that they do not result in the vanishing of the integrals of the slip gradient over the slip patches. Also an alternative set of integral conditions, proposed by [Weertman \(1996\)](#), leads to boundedness of the four slip gradient values at the boundaries but not to the required vanishing of the two integrals.

To obtain a solution with vanishing integrals of the slip gradient, and thus with vanishing end point values for the slip, we require two additional free parameters in the general inverse solution of the coupled Cauchy equation. Guided by results of [Bilby and Eshelby \(1968\)](#) and [Estrada and Kanwal \(2000\)](#), we showed that these parameters are provided by the integration constants of the homogeneous solution. These were stated to be always zero by [Muskhelishvili \(1953\)](#), but at least one of them obtains a finite value if the two integral conditions for the slip gradient are properly taken into account.

The reason for the in-applicability of the general solution of [Muskhelishvili \(1953\)](#) to our problem is that his text considers the formal inversion aspects of Cauchy equations, rather than the physical application to fault slip. In the latter, the relevant end-point conditions are given in terms of the slip, i.e., the integral of the slip gradient, rather than in terms of the slip gradient itself which forms the unknown variable in the Cauchy equation. The reason for the erroneous solution of [Weertman \(1996\)](#) is less clear but is probably the result of an a-priori assumption that the integration constants are equal to zero, in combination with a mistake in the contour integration procedure used by [Weertman \(1996\)](#).

The general inverse solution for the coupled two-patch problem thus requires six auxiliary conditions: four integral conditions over both patches (in terms of the pre-slip Coulomb stress, its first, second and third moment, and two integration constants), and two integral conditions over the individual slip patches (in terms of the slip gradient). Numerical evaluation shows that one of the integration constants is always non-zero whereas the other one vanishes for the examples considered. Moreover, it turns out to be possible to reduce these six conditions to four again, provided we are not interested in the values of the integration constant, but we stress that these four conditions are different from the ones obtained by [Muskhelishvili \(1953\)](#) and [Weertman \(1996\)](#).

Finally, we repeated the derivation for a coupled double-patch case with a symmetric pre-slip Coulomb stress pattern. In that case the general inverse solution requires three auxiliary conditions: two integral conditions over both patches (now in terms of the symmetric first and third moments of the pre-slip Coulomb stress, and the single integration constant), and one integral condition over one of the slip patches (in terms of the anti-symmetric slip gradient). Also now it turns out to be possible to reduce the number of conditions, in this case from three to two, provided we are not interested in the value of the integration constant.

To solve the various singular integrals in the “full method”, with six unknowns, and the “short-cut method”, with four unknowns, we employed a modified version of augmented Gauss–Chebyshev quadrature as originally proposed by [Erdogan and Gupta \(1972\)](#). The modification concerns the use of analytical inversion, prior to integration, which is as opposed to the original formulation which relies on numerical (matrix) inversion as part of the integration procedure.

We illustrated our findings with a numerical example of depletion-induced aseismic fault slip in a displaced normal fault. A comparison with fully numerical results, obtained with a finite-volume-based simulation package for poroelasticity, confirmed the validity of our semi-analytical coupled solution.

CRediT authorship contribution statement

Bernard Meulenbroek: Conceptualization, Formal analysis, Investigation, Methodology, Writing – original draft, Writing – review & editing. **Jan-Dirk Jansen:** Conceptualization, Formal analysis, Funding acquisition, Investigation, Methodology, Software, Validation, Writing – original draft, Writing – review & editing.

Declaration of competing interest

The authors declare that they have no known competing financial interests or personal relationships that could have appeared to influence the work reported in this paper.

Data availability

No data was used for the research described in the article.

Acknowledgments

This publication is part of the project ‘Science4Steer: a scientific basis for production and re-injection strategies to minimize induced seismicity in Dutch gas fields’ (with project number DEEP.NL.2018.046) of the research program ‘DeepNL’ which is financed by the Dutch Research Council (NWO), Netherlands. We thank Aleksei Novikov of TU Delft for performing the simulations to create the numerical results displayed in [Figs. 3 and 6](#).

Appendix A. Induced stresses

The material in Appendix A has largely been taken from [Jansen and Meulenbroek \(2022\)](#) except for [Appendix A.2](#), Eqs. (A.21) to (A.24), and the figures with the corresponding text.

A.1. Initial stresses

We assume the presence of an initial regional stress pattern with principal stresses σ_{yy}^0 (vertical) and

$$\begin{aligned}\sigma_{xx}^0 &= \sigma_{xx}^0 - \alpha p^0 \\ &= K^0 \sigma_{yy}^0 - \alpha p^0 \\ &= K^0(\sigma_{yy}^0 + \alpha p^0) - \alpha p^0,\end{aligned}\quad (\text{A.1})$$

(horizontal), where α is Biot’s coefficient (typically somewhat smaller than one), p^0 is the initial pore pressure (a superscript ‘0’ means ‘initial’), K^0 is the initial effective stress ratio, and where a primed stress variable σ' represents an ‘effective stress’. We employ the solid mechanics sign convention where positive strains and stresses imply extension and tension. The resulting initial normal and shear stresses acting on the fault follow from a coordinate rotation as

$$\sigma^0 = \sigma_{\bar{y}\bar{y}}^0 = \sigma_{xx}^0 \sin^2 \theta + \sigma_{yy}^0 \cos^2 \theta, \quad (\text{A.2})$$

$$\tau^0 = -\sigma_{\bar{x}\bar{y}}^0 = (\sigma_{xx}^0 - \sigma_{yy}^0) \sin \theta \cos \theta, \quad (\text{A.3})$$

where \bar{x} and \bar{y} are rotated coordinates, and where θ is the dip angle of the fault; see [Fig. 1](#). A positive-valued shear stress τ^0 corresponds to a normal faulting regime, i.e. a situation where the hanging wall (to the left of the fault in [Fig. 1](#)) has a tendency to slide down from the foot wall (to the right of the fault). The initial effective normal stress acting at the fault follows as

$$\sigma^0 = \sigma^0 + \beta p^0, \quad (\text{A.4})$$

where β is an effective stress coefficient which is not necessarily identical to α and is often taken as unity ([Scholz, 2019](#); [Fjaer et al., 2021](#)).

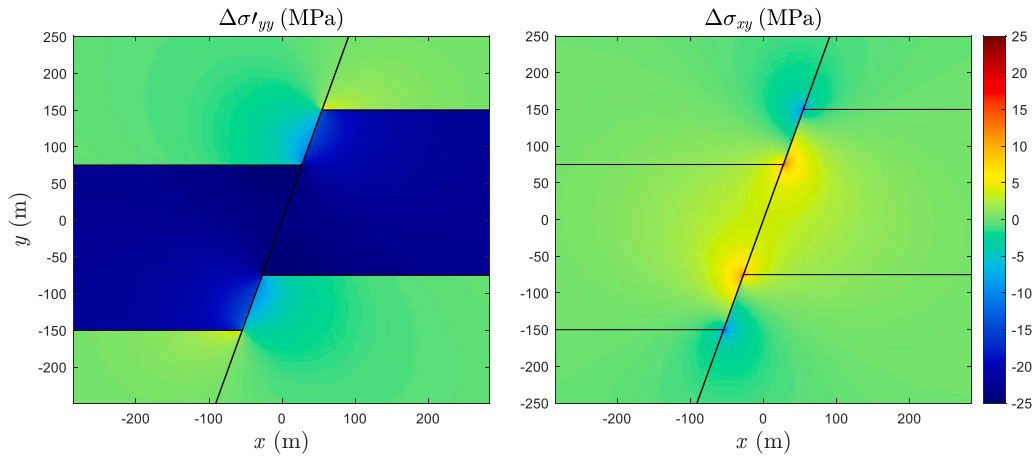


Fig. A.1. Incremental effective vertical stress $\Delta\sigma'_{yy}$ (left) and incremental shear stress $\Delta\sigma_{xy}$ (right) resulting from reservoir depletion for an example with parameter values given in Table 1. Note that the color bar has a limited range and therefore does not completely represent the shear stress levels which reach (mathematically) positive and negative infinite values at the internal and external reservoir-fault corners respectively.

A.2. Incremental stresses

An increase or decrease in pore pressure in the reservoir will result in incremental normal and shear stresses in the reservoir and its surroundings because of poroelastic effects (Biot, 1941; Segall, 1989; Wang, 2000). We restrict the analysis in this paper to the case of a quasi steady state, i.e. a spatially homogeneous incremental pore pressure $\Delta p(t)$ that is a slow function of time t . Using a technique known as *inclusion theory* it is possible to compute the incremental strains and stresses, inside and outside the reservoir, that result from a change in reservoir pore pressure Δp (Segall, 1985, 1989; Rudnicki, 2011; Cornelissen et al., 2024). For the depletion example with parameter values given in Table 1, Fig. A.1 (left) displays the effective change in vertical stress $\Delta'\sigma_{yy}$, defined as

$$\Delta\sigma'_{yy} = \Delta\sigma_{yy} + \alpha\Delta p, \quad (\text{A.5})$$

where $\Delta\sigma_{yy}$ is the total change in vertical stress, caused by poroelastic effects. The incremental pore pressure Δp is negative and so is the value of $\Delta\sigma'_{yy}$, implying compressive stresses in the grains leading to vertical compaction. In those parts of the fault where reservoir rock juxtaposes non-reservoir rock, i.e. for $-b < y < -a$ and $a < y < b$ with $a = 75$ m and $b = 150$ m, the vertical compaction in the reservoir rock is hampered by the stiffness of the adjacent non-reservoir rock. As a result, severe shear stresses develop which, theoretically, reach peak values of infinite magnitude at the internal and external reservoir-fault corners as displayed in Fig. A.1 (right).

A.3. Closed-form expressions

Closed-form analytical expressions for incremental normal and shear stresses in a displaced fault were obtained by Jansen et al. (2019) with the aid of inclusion theory and can be expressed as

$$\Delta\sigma = (-\Delta\sigma_{xy} \sin\theta \cos\theta + \Delta\sigma_{xx} \sin^2\theta), \quad (\text{A.6})$$

$$\Delta\tau = (\Delta\sigma_{xy} \sin^2\theta + \Delta\sigma_{xx} \sin\theta \cos\theta), \quad (\text{A.7})$$

where $\Delta\sigma_{xx} = \Delta\sigma_{\bar{y}\bar{y}}$ and $\Delta\sigma_{xy} = -\Delta\sigma_{\bar{x}\bar{y}}$ are normal and shear stresses in a vertical fault, i.e. for a dip angle $\theta = \frac{\pi}{2}$. For an infinitely wide reservoir, they are defined as (see also Appendix A in Jansen and Meulenbroek (2022))

$$\Delta\sigma_{xx} = \begin{cases} 0 & \text{if } y \leq -b \text{ or } b \leq y \\ -\pi C & \text{if } -b < y \leq -a \text{ or } a \leq y < b, \\ -2\pi C & \text{if } -a < y < a \end{cases} \quad (\text{A.8})$$

and

$$\Delta\sigma_{xy} = \frac{C}{2} \ln \frac{(y-a)^2(y+a)^2}{(y-b)^2(y+b)^2}, \quad (\text{A.9})$$

where C is a pressure-dependent scaling parameter, with SI units Newton per meter squared, defined as

$$C = \frac{(1-2\nu)\alpha\Delta p(t)}{2\pi(1-\nu)}, \quad (\text{A.10})$$

with ν representing Poisson's ratio. For dipping as well as vertical faults the incremental effective normal stress is given by

$$\Delta\sigma' = \Delta\sigma + \begin{cases} 0 & \text{if } y \leq -b \text{ or } b \leq y \\ \beta\Delta p & \text{if } -b < y < b \end{cases}. \quad (\text{A.11})$$

In the derivation of Eq. (A.11) it was assumed that only those parts of the fault that are in direct contact with the reservoir experience incremental reservoir pressure, i.e. that the relevant fault segment is given by $-b < y < b$. If a larger part of the fault is exposed to incremental pressure, the domain where $\beta\Delta p$ is added should be extended accordingly.

Somewhat more elaborate closed-form expressions for a finite-width reservoir, derived with inclusion theory, are given in the paper by Jansen et al. (2019) and the accompanying Supporting Information. These can also be used to obtain the stresses in case of a fully sealing fault with different reservoir pressures to the left and the right of the fault. Moreover, if the width of the reservoir section to either side of the fault is taken as zero, these expressions describe the stresses in a bounding fault, or a sealing fault with zero depletion at one of the sides in which case only two shear stress peaks occur — one positive and one negative. Similar expression were published concurrently by Lehner (2019) and later by Wu et al. (2021), while some mathematical subtleties in these publications were recently discussed by Cornelissen et al. (2024). We note that the expressions that follow from inclusion theory can also be derived from potential theory, which is closely related to the nucleus of strain concept, and we refer to Rudnicki (2002) and Rudnicki (2011) for further details.

In case of a non-homogeneous pressure field, inclusion theory can still be applied to obtain the fault stresses but the resulting integrals have to be solved numerically, an approach that has been followed early-on by Segall (1985), and later by several other authors; see Cornelissen et al. (2024) for an overview of various recent 2D and 3D applications.

A.4. Fault slip and Coulomb stress

Fault slip is defined as

$$\delta(s, t) = u^+(s, t) - u^-(s, t), \quad (\text{A.12})$$

where s is the along-fault coordinate while u^- and u^+ are the along-fault displacements at both sides of the fault. Fault slip is governed by the combined (i.e. initial plus incremental) shear and effective normal stresses

$$\tau = \tau^0 + \Delta\tau, \quad (\text{A.13})$$

$$\sigma' = \sigma'^0 + \Delta\sigma'. \quad (\text{A.14})$$

Slip-provoking conditions occur when

$$|\tau| > \tau_{sl}, \quad (\text{A.15})$$

where τ_{sl} is the slip threshold, defined as

$$\tau_{sl} = \kappa - \mu\sigma', \quad \kappa \geq 0, \quad \sigma' < 0, \quad (\text{A.16})$$

with κ indicating cohesion and μ the friction coefficient, and where it should be kept in mind that negative (effective) normal stresses correspond to compression.

Eq. (A.15) implies that slip of the hanging wall may occur in upward or downward direction, where exceedance of the slip threshold τ_{sl} by a positive combined shear stress τ implies downward slip of the hanging wall, i.e. a continued normal fault development. In this paper we only consider such downward slip without reversals of direction and therefore employ the usual definition of the pre-slip Coulomb stress

$$\tau_C = \tau - \tau_{sl}, \quad (\text{A.17})$$

in which slip corresponds to positive values of τ_C .

A.5. Regularized expressions

Eqs. (A.6) and (A.7) for the incremental stresses contain logarithmic singularities and jump discontinuities at $y = \pm a$ and $y = \pm b$. A regularized form of the incremental stresses removes the singularities and discontinuities; see Appendix B in Jansen and Meulenbroek (2022). We quote the following expressions from that appendix:

$$\Delta\sigma'_{xx} = -C \left\{ \arctan 2 \left[(a+b)\eta, \eta^2 + (y-b)(y+a) \right] + \arctan 2 \left[(a+b)\eta, \eta^2 + (y-a)(y+b) \right] \right\}, \quad (\text{A.18})$$

$$\Delta\sigma'_{xy} = \frac{C}{2} \ln \frac{[\eta^2 + (y-a)^2][\eta^2 + (y+a)^2]}{[\eta^2 + (y-b)^2][\eta^2 + (y+b)^2]}, \quad (\text{A.19})$$

where the 'arctan2' operation is defined for arguments (y, x) in the interval $[-\pi, \pi]$ according to

$$\arctan 2(y, x) = \begin{cases} \operatorname{sgn}(y) \cdot \arctan\left(\left|\frac{y}{x}\right|\right) & x > 0 \\ \operatorname{sgn}(y) \cdot \frac{\pi}{2} & x = 0, y \neq 0 \\ \text{undefined} & x = 0, y = 0 \\ \operatorname{sgn}(y) \cdot \left[\pi - \arctan\left(\left|\frac{y}{x}\right|\right)\right] & x < 0 \end{cases} \quad (\text{A.20})$$

Eqs. (A.18) and (A.19) can be used instead of Eqs. (A.8) and (A.9) to which they can be shown to revert for $\eta = 0$. The corresponding regularized version of the second line in Eq. (A.11) for the effective normal stresses is given by

$$\Delta\sigma'' = \Delta\sigma + \beta\Delta p^r = \Delta\sigma + \beta\frac{\Delta p}{\pi} \arctan 2 \left[2b\eta, \eta^2 + (y-b)(y+b) \right]. \quad (\text{A.21})$$

Eq. (A.21) contains a small correction of the original expression for $\Delta\sigma''$ in Jansen and Meulenbroek (2022): the first term inside the square brackets was originally taken as $(a+b)\eta$ whereas here we use $2b\eta$. In numerical examples the difference is hardly noticeable, but the current formulation is internally consistent, as demonstrated in the next paragraph, whereas the original formulation was not.

Both the unregularized and the regularized expressions can be integrated analytically and it can be shown that

$$\int_{-\infty}^{\infty} \Delta\sigma'_{xx}(y) dy = \int_{-\infty}^{\infty} \Delta\sigma''_{xx}(y) dy = 2\pi C(a+b), \quad (\text{A.22})$$

$$\int_{-\infty}^{\infty} \Delta\sigma'_{xy}(y) dy = \int_{-\infty}^{\infty} \Delta\sigma''_{xy}(y) dy = 0, \quad (\text{A.23})$$

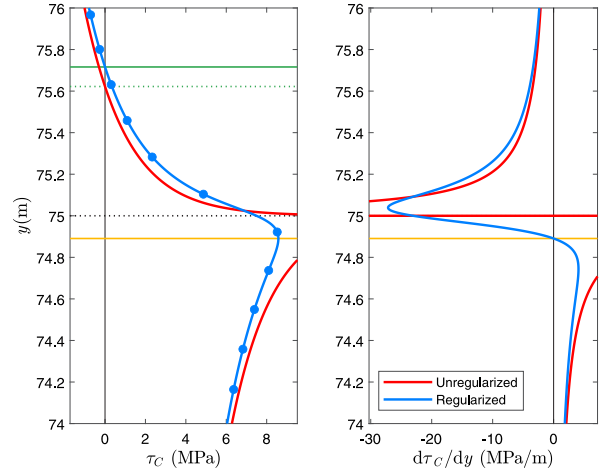


Fig. A.2. Pre-slip Coulomb stress τ_C (left) and its spatial derivative $\frac{d\tau_C}{dy}$ (right) with and without regularization, in the neighborhood the singularity at $y = a = 75.0$ m (dotted black line) which coincides with one of the four infinite-magnitude peaks of the unregularized version of τ_C . The orange horizontal line at $y = 74.9$ m corresponds to the local zero of the regularized version of $\frac{d\tau_C}{dy}$ and therefore to the (finite) local maximum of the regularized version of τ_C . The figure has been produced with parameter values from Table 1, and the value of the regularization parameter is $\eta = 0.10$ m. As a result of the regularization the location of the maximum value of τ_C has shifted over approximately the same distance. The same holds for the shift in location of the pre-slip Coulomb stress zeros; see the solid (regularized) and dotted (unregularized) green lines in the left plot. The blue dots in the left figure illustrate the location of the Chebyshev points for a number of points per slip patch $N_k = 256$.

$$\int_{-\infty}^{\infty} \Delta p(y) dy = \int_{-\infty}^{\infty} \Delta p^r(y) dy = 2b\beta\Delta p. \quad (\text{A.24})$$

which implies that the regularization has only a local effect that does not disturb the global stress distribution in the fault. Also differentiation of the regularized expressions can be done analytically and the result for values around one of the infinite peaks in the pre-slip Coulomb stress has been displayed in Fig. A.2 (right). The corresponding maximum of the pre-slip Coulomb stress, depicted in Fig. A.2 (left), displays a small shift in location, of the same order of magnitude as the value of the regularization parameter η . A similar small shift is observed in the location of the pre-slip Coulomb stress zeros.

In the numerical example in our paper we used $\eta = 0.10$ m and we employed around 250 grid points per slip patch in the numerical integration procedure to resolve the corresponding smoothed peaks; see Fig. A.2 (left). Reducing the value of η leads to convergence of the results but at the cost of an increased number of grid points to resolve the peaks.

Appendix B. Inverse Cauchy equations over neighboring intervals

B.1. Problem statement

We aim to derive the inverse expression of Eq. (13) which is a Cauchy-type singular integral over a domain L consisting of two separate line intervals on the real axis:

$$\text{PV} \int_L \frac{g(\xi)}{\xi - y} d\xi = f(y), \quad L = L_1 \cup L_2 \equiv (\tilde{y}_1, \tilde{y}_2) \cup (\tilde{y}_3, \tilde{y}_4), \quad (\text{B.1})$$

where we introduced a generic notation to indicate the functions $f(y)$ and $g(y)$ which are known and unknown respectively. For the case of a two-interval Cauchy integral with pre-slip Coulomb stresses τ_C we have the following equivalencies:

$$f(y) \equiv -\tau_C(y)/A, \quad (\text{B.2})$$

$$g(y) \equiv \nabla\delta(y). \quad (\text{B.3})$$

while the two line intervals represent slip patches. Just like in the main text we will refrain from indicating the principal value (PV) explicitly in the remainder of this Appendix. Eq. (B.1) describes a mixed boundary value problem in which $f(y)$ is prescribed for $y \in L$ and $g(y) = 0$ for $y \notin L$. Moreover, it is a free boundary problem, in the sense that we do not a-priori know the location of the end points $\bar{y}_i, i = 1, \dots, 4$, and need additional conditions to determine them.

Following equation (3.155) of Estrada and Kanwal (2000) the inverse of Eq. (B.1) can be expressed as

$$g(y) = \frac{1}{\pi^2 \Psi_{\pm}(y)} \int_L \frac{\Psi_{\pm}(\xi) f(\xi)}{y - \xi} d\xi + \frac{C_0 + C_1 y}{\pi^2 \Psi_{\pm}(y)}, \quad (B.4)$$

where

$$\Psi_{\pm}(y) = \pm \sqrt{-(y - \bar{y}_1)(y - \bar{y}_2)(y - \bar{y}_3)(y - \bar{y}_4)}, \quad (B.5)$$

and where the plus and minus signs preceding the square root term correspond to $y \in L_2$ and $y \in L_1$ respectively. Note that in this formulation the square root is always real, as defined in equation (3.152) of Estrada and Kanwal (2000). Also note that, unlike here, in Estrada and Kanwal (2000) the dependent and independent variables (y and ξ) are swapped when going from the ‘forward’ to the ‘inverse’ expression (Eqs. (B.1) and (B.4)), while the terms $\xi - y$ and $y - \xi$ in the denominators are identical to those in our formulation, resulting in a sign change in Eq. (B.4).

The last term in Eq. (B.4) is the solution of the homogeneous version of Eq. (B.1):

$$\int_L \frac{g(\xi)}{\xi - y} d\xi = 0, \quad (B.6)$$

while the integral term in Eq. (B.4) is a particular solution for the right-hand side $f(y)$ in Eq. (B.1).

B.2. Conditions for a bounded solution at all endpoints

The terms $1/\Psi_{\pm}(y)$ in Eq. (B.4) become unbounded for $y \in \{\bar{y}_1, \bar{y}_2, \bar{y}_3, \bar{y}_4\}$. To obtain a solution that remains bounded in the four end points we follow the approach that Bilby and Eshelby (1968) used for a single-interval problem, and introduce the identity

$$\frac{\Psi(\xi)}{\Psi(y)} - \frac{\Psi(y)}{\Psi(\xi)} = \frac{\Psi^2(\xi) - \Psi^2(y)}{\Psi(\xi)\Psi(y)}, \quad (B.7)$$

where we temporarily drop the subscript \pm . The nominator of the right-hand side of this expression can be rewritten as

$$\Psi^2(\xi) - \Psi^2(y) = (y - \xi)(A_0 + A_1 y + A_2 y^2 + A_3 y^3), \quad (B.8)$$

where

$$A_0 = B_0 + B_1 \xi + B_2 \xi^2 + B_3 \xi^3, \quad (B.9)$$

$$A_1 = B_1 + B_2 \xi + B_3 \xi^2, \quad (B.10)$$

$$A_2 = B_2 + B_3 \xi, \quad (B.11)$$

$$A_3 = B_3, \quad (B.12)$$

$$B_0 = -(\bar{y}_1 \bar{y}_2 \bar{y}_3 + \bar{y}_1 \bar{y}_2 \bar{y}_4 + \bar{y}_1 \bar{y}_3 \bar{y}_4 + \bar{y}_2 \bar{y}_3 \bar{y}_4) \quad (B.13)$$

$$B_1 = \bar{y}_1 \bar{y}_2 + \bar{y}_1 \bar{y}_3 + \bar{y}_1 \bar{y}_4 + \bar{y}_2 \bar{y}_3 + \bar{y}_2 \bar{y}_4 + \bar{y}_3 \bar{y}_4 \quad (B.14)$$

$$B_2 = -(\bar{y}_1 + \bar{y}_2 + \bar{y}_3 + \bar{y}_4) \quad (B.15)$$

$$B_3 = 1, \quad (B.16)$$

With the aid of Eqs. (B.7) to (B.16) we can now rewrite Eq. (B.4) as

$$g(y) = \frac{\Psi_{\pm}(y)}{\pi^2} \int_L \frac{f(\xi)}{\Psi_{\pm}(\xi)(y - \xi)} d\xi + \frac{D_0 + D_1 y + D_2 y^2 + D_3 y^3}{\pi^2 \Psi_{\pm}(y)} + \frac{C_0 + C_1 y}{\pi^2 \Psi_{\pm}(y)}, \quad (B.17)$$

where

$$D_0 = B_0 I_0 + B_1 I_1 + B_2 I_2 + B_3 I_3, \quad (B.18)$$

$$D_1 = B_1 I_0 + B_2 I_1 + B_3 I_2, \quad (B.19)$$

$$D_2 = B_2 I_0 + B_3 I_1, \quad (B.20)$$

$$D_3 = B_3 I_0, \quad (B.21)$$

with

$$I_i = \int_L \frac{y^i f(y)}{\Psi_{\pm}(y)} dy = \int_{L_1} \frac{y^i f(y)}{\Psi_{-}(y)} dy + \int_{L_2} \frac{y^i f(y)}{\Psi_{+}(y)} dy, \quad i = 0, \dots, 3. \quad (B.22)$$

For $g(y)$ to be bounded in the four end points it is necessary that the sum of the last two terms at the right-hand side of Eq. (B.17) vanishes. Because the four unknown coefficients $D_i(\bar{y}_{1,\dots,4}), i = 0, \dots, 3$, are functions of the four end points $\bar{y}_1, \dots, \bar{y}_4$, this implies that the end points should be selected such that

$$C_0 + D_0 = 0, \quad (B.23)$$

$$C_1 + D_1 = 0, \quad (B.24)$$

$$D_2 = 0, \quad (B.25)$$

$$D_3 = 0. \quad (B.26)$$

With the aid of Eqs. (B.15) and (B.18) to (B.21), conditions (B.23) to (B.26) can also be expressed as

$$C_0 + (\bar{y}_1 + \bar{y}_2 + \bar{y}_3 + \bar{y}_4)C_1 + I_3 = 0, \quad (B.27)$$

$$C_1 + I_2 = 0, \quad (B.28)$$

$$I_1 = 0, \quad (B.29)$$

$$I_0 = 0. \quad (B.30)$$

The unknown coefficients C_0 and C_1 can be obtained by imposing two conditions on the general solution. In particular, we require the integral of the slip gradient $\nabla \delta$ over each of the patches to vanish which can be represented in the generic notation of this Appendix as:

$$\int_{L_1} g(y) dy = 0, \quad (B.31)$$

$$\int_{L_2} g(y) dy = 0. \quad (B.32)$$

With Eq. (B.4) this can be expressed as

$$\int_{L_1} \frac{1}{\Psi_{-}(y)} \int_L \frac{\Psi_{\pm}(\xi) f(\xi)}{y - \xi} d\xi dy + \int_{L_1} \frac{C_0 + C_1 y}{\Psi_{-}(y)} dy = 0, \quad (B.33)$$

$$\int_{L_2} \frac{1}{\Psi_{+}(y)} \int_L \frac{\Psi_{\pm}(\xi) f(\xi)}{y - \xi} d\xi dy + \int_{L_2} \frac{C_0 + C_1 y}{\Psi_{+}(y)} dy = 0, \quad (B.34)$$

which can be rewritten as a linear system of equations

$$\begin{bmatrix} A_{11} & A_{12} \\ A_{21} & A_{22} \end{bmatrix} \begin{bmatrix} C_0 \\ C_1 \end{bmatrix} = \begin{bmatrix} b_1 \\ b_2 \end{bmatrix}, \quad (B.35)$$

where

$$A_{11} = \int_{L_1} \frac{1}{\Psi_{-}(y)} dy, \quad (B.36)$$

$$A_{12} = \int_{L_1} \frac{y}{\Psi_{-}(y)} dy, \quad (B.37)$$

$$A_{21} = \int_{L_2} \frac{1}{\Psi_{+}(y)} dy, \quad (B.38)$$

$$A_{22} = \int_{L_2} \frac{y}{\Psi_{+}(y)} dy, \quad (B.39)$$

$$b_1 = - \int_{L_1} \frac{1}{\Psi_{-}(y)} \int_L \frac{\Psi_{\pm}(\xi) f(\xi)}{y - \xi} d\xi dy, \quad (B.40)$$

$$b_2 = - \int_{L_2} \frac{1}{\Psi_{+}(y)} \int_L \frac{\Psi_{\pm}(\xi) f(\xi)}{y - \xi} d\xi dy. \quad (B.41)$$

The solution procedure now consists of iteratively searching for the four values $\bar{y}_1, \dots, \bar{y}_4$ that make the four conditions (B.23) to (B.26) (or conditions (B.27) to (B.30)) equal to zero. During each iteration step the unknowns C_0 and C_1 have to be obtained by solving the 2×2 linear system (B.35).

Evaluation of numerical examples reveals that C_0 always has a non-zero value while C_1 is always (numerically) equal to zero. Straight-forward determination of the conditions under which C_1 vanishes seems to be out of reach. Although some of the governing integrals can be solved in terms of elliptic integrals, the presence of singularities, and therefore the need to use principal values, requires an analysis beyond the scope of the current paper. Because the vanishing of C_1 does not influence the main conclusions, we leave a further investigation of this numerical finding as material for future research.

With $C_1 = 0$, the solution of the 2×2 system (B.35) reduces to

$$C_0 = \frac{A_{22}b_1 - A_{12}b_2}{A_{12}A_{21} - A_{11}A_{22}}. \quad (B.42)$$

Alternatively, one could use either Eq. (B.33) or (B.34) with $C_1 = 0$ to solve for C_0 .

B.3. Alternative formulation

Instead of using the six conditions (B.23) to (B.32) to determine the four end points $\tilde{y}_1, \dots, \tilde{y}_4$ and the two coefficients C_0 and C_1 , we can use four alternative conditions to determine the four end points directly, without the need to compute C_0 and C_1 . Note that we continue the use of C_1 as an unknown parameter, to remain aligned with the derivation above. In practice, one may want to set $C_1 = 0$ a priori.

We now use expression (B.17) for $g(y)$ instead of expression (B.4) and we first choose the free variables C_0 and C_1 such that

$$C_0 + D_0 = 0, \quad C_1 + D_1 = 0, \quad (B.43)$$

in terms of the (at this point unknown) parameters $\tilde{y}_1, \dots, \tilde{y}_4$. This means that Eq. (B.17) now reduces to

$$g(y) = \frac{\Psi_{\pm}(y)}{\pi^2} \int_L \frac{f(\xi)}{\Psi_{\pm}(\xi)(y-\xi)} d\xi + \frac{D_2y^2 + D_3y^3}{\pi^2\Psi_{\pm}(y)}. \quad (B.44)$$

In order to have a finite slip gradient at the endpoints, we need to impose the conditions

$$D_2 = 0, \quad D_3 = 0, \quad (B.45)$$

or, equivalently,

$$I_1 = 0, \quad I_0 = 0, \quad (B.46)$$

and in order to satisfy conditions (B.31) and (B.32) (the integral of the slip gradient $\nabla\delta$ has to vanish over both patches) we need to impose furthermore the conditions

$$\int_{L_1} \frac{\Psi_{-}(y)}{\pi^2} \int_L \frac{f(\xi)}{\Psi_{\pm}(\xi)(y-\xi)} d\xi dy = 0, \quad (B.47)$$

$$\int_{L_2} \frac{\Psi_{+}(y)}{\pi^2} \int_L \frac{f(\xi)}{\Psi_{\pm}(\xi)(y-\xi)} d\xi dy = 0, \quad (B.48)$$

where we used expression (B.44) with conditions (B.46) for $g(y)$. In summary, this leads to the four conditions

$$\int_{L_1} \Psi_{-}(y) \int_L \frac{f(\xi)}{\Psi_{\pm}(\xi)(y-\xi)} d\xi dy = 0, \quad (B.49)$$

$$\int_{L_2} \Psi_{+}(y) \int_L \frac{f(\xi)}{\Psi_{\pm}(\xi)(y-\xi)} d\xi dy = 0, \quad (B.50)$$

$$I_1 = 0, \quad (B.51)$$

$$I_0 = 0, \quad (B.52)$$

that determine the end point values $\tilde{y}_1, \dots, \tilde{y}_4$.

An alternative ‘‘short-cut’’ solution procedure now consists of iteratively searching for the four values $\tilde{y}_1, \dots, \tilde{y}_4$ that make the four alternative conditions (B.49) to (B.52) equal to zero. The two unknown coefficients C_0 and C_1 can then, in theory, be obtained from the original conditions (B.23) and (B.24) after computing D_0 and D_1 with the aid of Eqs. (B.13) to (B.16), (B.18) and (B.19). In practice, however, we do no longer need those two coefficients in the iterative

procedure. Fig. B.1 depicts the values of the non-zero coefficient C_0 for the full formulation (red solid curves) and the alternative (short-cut) formulation (dashed blue curve), for the example considered in the main text. It can be seen that the curves exactly overlap. The computational speed of the alternative formulation is slightly higher than of the original one. However, for the numerical examples that we considered, the alternative formulation turned out to be somewhat more prone to numerical (integration) errors and occasionally resulted in inaccurate values for the slip patch boundaries.

B.4. Single patch

When coupling effects are neglected, or when the two slip patches have merged, the problem statement (B.1) reduces to

$$\int_L \frac{g(\xi)}{\xi - y} d\xi = f(y), \quad L = (\tilde{y}_-, \tilde{y}_+), \quad (B.53)$$

where $(\tilde{y}_-, \tilde{y}_+) = (\tilde{y}_1, \tilde{y}_2)$ for the bottom patch, $(\tilde{y}_-, \tilde{y}_+) = (\tilde{y}_3, \tilde{y}_4)$ for the top patch, and $(\tilde{y}_-, \tilde{y}_+) = (\tilde{y}_1, \tilde{y}_4)$ for merged patches. Following equation (3.155) of Estrada and Kanwal (2000) again, the inverse of Eq. (B.53) can be expressed as

$$g(y) = \frac{1}{\pi^2\Phi(y)} \int_L \frac{\Phi(\xi)f(\xi)}{\xi - y} d\xi + \frac{C_0}{\pi^2\Phi(y)}, \quad (B.54)$$

where

$$\Phi(y) = \sqrt{-(y - \tilde{y}_-)(y - \tilde{y}_+)}. \quad (B.55)$$

To guarantee a bounded solution we pursue the same approach as for the two-patch case and write, keeping the same notation,

$$\frac{\Phi(\xi)}{\Phi(y)} - \frac{\Phi(y)}{\Phi(\xi)} = \frac{\Phi^2(\xi) - \Phi^2(y)}{\Phi(\xi)\Phi(y)}, \quad (B.56)$$

The nominator of the right-hand side of this expression can be rewritten as

$$\Phi^2(\xi) - \Phi^2(y) = (y - \xi)(A_0 + A_1y), \quad (B.57)$$

where

$$A_0 = B_0 + B_1\xi, \quad (B.58)$$

$$A_1 = B_1, \quad (B.59)$$

$$B_0 = -(\tilde{y}_- + \tilde{y}_+), \quad (B.60)$$

$$B_1 = 1, \quad (B.61)$$

With the aid of Eqs. (B.56) to (B.61) we can now rewrite Eq. (B.54) as

$$g(y) = \frac{\Phi(y)}{\pi^2} \int_L \frac{f(\xi)}{\Phi(\xi)(y-\xi)} d\xi + \frac{D_0 + D_1y}{\pi^2\Phi(y)} + \frac{C_0}{\pi^2\Phi(y)}, \quad (B.62)$$

where

$$D_0 = B_0I_0 + B_1I_1, \quad (B.63)$$

$$D_1 = B_1I_0, \quad (B.64)$$

with

$$I_i = \int_L \frac{y^i f(y)}{\Phi(y)} dy, \quad i = 0, 1. \quad (B.65)$$

For $g(y)$ to be unbounded in the two end points we now obtain the conditions

$$C_0 + D_0 = 0, \quad (B.66)$$

$$D_1 = 0, \quad (B.67)$$

The unknown coefficient C_0 can again be obtained by imposing a condition on the general solution. In particular, we require

$$\int_L g(y) dy = 0. \quad (B.68)$$

With Eq. (B.54) the integral in condition (B.68) can be written as

$$\int_L g(y) dy = \int_L \left(\frac{1}{\pi^2\Phi(y)} \int_L \frac{\Phi(\xi)f(\xi)}{\xi - y} d\xi + \frac{C_0}{\pi^2\Phi(y)} \right) dy$$

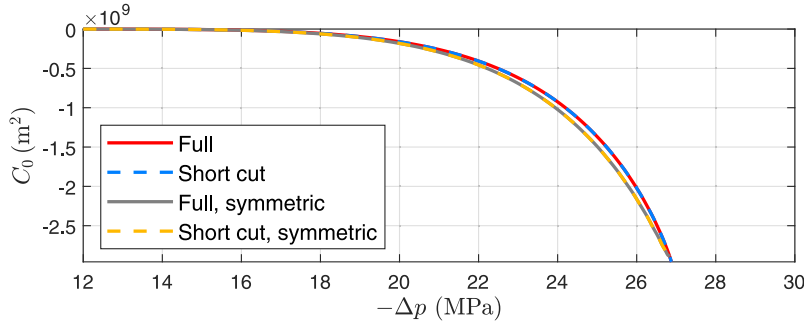


Fig. B.1. Coefficient C_0 for different formulations.

$$= \frac{1}{\pi^2} \left(\int_L \int_L \frac{\Phi(\xi)f(\xi)}{\Phi(y)(\xi-y)} dy d\xi + \int_L \frac{C_0}{\Phi(y)} dy \right) = \frac{C_0}{\pi}, \quad (\text{B.69})$$

where we made use of the integrals

$$\int_L \frac{1}{\Phi(y)(\xi-y)} dy = 0, \quad (\text{B.70})$$

$$\int_L \frac{1}{\Phi(y)} dy = \pi, \quad (\text{B.71})$$

(Estrada and Kanwal, 2000; Jansen and Meulenbroek, 2022, Supporting Information, eqs. (S.2.10) and (S.2.13)). Therefore, in this single-patch case, we find $C_0 = 0$ which implies that the homogeneous solution is uncoupled from the general solution. This is an essential difference with the double-patch case where the two solutions are coupled, in which case the computation of the integration constants C_0 and C_1 requires solving six requirements simultaneously. Here we find that conditions (B.66) and (B.67) reduce to

$$D_0 = D_1 = 0, \quad (\text{B.72})$$

or, equivalently,

$$I_i = \int_L \frac{y^i f(y)}{\Phi(y)} dy = 0, \quad i = 0, 1. \quad (\text{B.73})$$

B.5. Earlier conditions

As discussed in the main text, Muskhelishvili (1953) and Weertman (1996) both presented four conditions for the boundedness of the two-patch case. Both authors set $C_0 = C_1 = 0$ a priori. However, as discussed in the previous section, this not necessarily correct. Muskhelishvili then obtained

$$I_i^M = \int_L \frac{y^i f(y)}{\Psi_{\pm}(y)} dy = 0, \quad i = 0, \dots, 3, \quad (\text{B.74})$$

which is identical to our conditions (B.27) to (B.30) but with vanishing C_0 and C_1 , although there is some ambiguity in the counters in the original text (Muskhelishvili, 1953, Eq. (88).10). Weertman arrived at the same result except for a slightly different fourth condition (Weertman, 1996, Eq. (3).45):

$$I_i^W = \int_L \frac{y^i f(y)}{\Psi_{\pm}(y)} dy = 0, \quad i = 0, \dots, 2, \quad (\text{B.75})$$

$$I_3^W = \int_L \frac{y|y|f(y)}{\Psi_{\pm}(y)} dy = 0. \quad (\text{B.76})$$

Both sets of conditions do indeed lead to bounded solutions for the slip gradient which, however, fail to adhere to the additional conditions (B.31) and (B.32) which represent the physical requirement that the integral of the slip gradient over each of the slip patches vanishes.

B.6. Symmetry

In this section we will compute $g(y)$ for a symmetric single slip patch with $\bar{y}_1 = -\bar{y}_4$, as occurs after merging, and for a symmetric double-patch configuration with $\bar{y}_1 = -\bar{y}_4$ and $\bar{y}_2 = -\bar{y}_3$. We will show that the single-patch solution is the limit of the double-patch solution for $\bar{y}_3 \rightarrow 0$.

B.6.1. Single patch

If $f(-y) = f(y)$, Eq. (B.53) can be rewritten as

$$\begin{aligned} f(y) = f(-y) &= \int_{\bar{y}_1}^{\bar{y}_4} \frac{g(\xi)}{\xi+y} d\xi = \int_{-\bar{y}_1}^{-\bar{y}_4} \frac{g(-\tau)}{-\tau+y} d(-\tau) \\ &= \int_{\bar{y}_4}^{-\bar{y}_1} \frac{g(-\tau)}{-\tau+y} d(-\tau) = \int_{-\bar{y}_4}^{\bar{y}_1} \frac{g(\xi)}{\xi+y} d\xi. \end{aligned} \quad (\text{B.77})$$

Defining a symmetric version of Eq. (B.55) as

$$\tilde{\Phi}(y) = \sqrt{-(y+\bar{y}_4)(y-\bar{y}_4)} = \sqrt{\bar{y}_4^2 - y^2}, \quad (\text{B.78})$$

we can therefore rewrite Eq. (B.62) as

$$\begin{aligned} g(y) &= \frac{\tilde{\Phi}(y)}{\pi^2} \int_{-\bar{y}_4}^{\bar{y}_4} \frac{f(\xi)}{\tilde{\Phi}(\xi)(y-\xi)} d\xi \\ &= \frac{\tilde{\Phi}(y)}{\pi^2} \left(\int_0^{\bar{y}_4} \frac{f(\xi)}{\tilde{\Phi}(\xi)(y-\xi)} d\xi + \int_{-\bar{y}_4}^0 \frac{f(\xi)}{\tilde{\Phi}(\xi)(y-\xi)} d\xi \right) \\ &= \frac{\tilde{\Phi}(y)}{\pi^2} \int_0^{\bar{y}_4} \frac{f(\xi)}{\tilde{\Phi}(\xi)} \left(\frac{1}{y-\xi} + \frac{1}{y+\xi} \right) d\xi \\ &= \frac{2y\tilde{\Phi}(y)}{\pi^2} \int_0^{\bar{y}_4} \frac{f(\xi)}{\tilde{\Phi}(\xi)(y^2 - \xi^2)} d\xi, \end{aligned} \quad (\text{B.79})$$

where we used our knowledge from the asymmetric single-patch case that $C_0 = 0$. Eqs. (B.65) become

$$I_1 = \int_{\bar{y}_1}^{\bar{y}_4} \frac{yf(y)}{\tilde{\Phi}(y)} dy = \int_{-\bar{y}_4}^{\bar{y}_4} \frac{yf(y)}{\tilde{\Phi}(y)} dy = 0, \quad (\text{B.80})$$

because the integrand is anti-symmetric, and

$$I_0 = \int_{\bar{y}_1}^{\bar{y}_4} \frac{f(y)}{\tilde{\Phi}(y)} dy = \int_0^{\bar{y}_4} \frac{2f(y)}{\tilde{\Phi}(y)} dy, \quad (\text{B.81})$$

because the integrand is symmetric, which means that the boundary point \bar{y}_4 is determined by the equation

$$\int_0^{\bar{y}_4} \frac{f(y)}{\tilde{\Phi}(y)} dy = 0, \quad (\text{B.82})$$

which now replaces Eq. (B.73).

B.6.2. Double patch

With $0 < \bar{y}_3, 0 < \bar{y}_4, \bar{y}_1 = -\bar{y}_4 < 0$ and $\bar{y}_2 = -\bar{y}_3 < 0$, the symmetric version of Eq. (B.5) becomes

$$\tilde{\Psi}_{\pm}(y) = \pm \sqrt{-(y+\bar{y}_4)(y+\bar{y}_3)(y-\bar{y}_3)(y-\bar{y}_4)} = \pm \sqrt{(y^2 - \bar{y}_3^2)(\bar{y}_4^2 - y^2)}, \quad (\text{B.83})$$

with the plus and minus signs preceding the square root term corresponding to $y > 0$ and $y < 0$ respectively. Following similar steps as for the single patch, Eq. (B.17) can now be rewritten as

$$g(y) = \frac{\tilde{\Psi}_{\pm}(y)}{\pi^2} \int_{\bar{y}_3}^{\bar{y}_4} \frac{2\xi f(\xi)}{\tilde{\Psi}_{\pm}(\xi)(y^2 - \xi^2)} d\xi + \frac{D_0 + D_2 y^2}{\pi^2 \tilde{\Psi}_{\pm}(y)} + \frac{C_0}{\pi^2 \tilde{\Psi}_{\pm}(y)}. \quad (\text{B.84})$$

Here we used the result that B_1 and B_3 as defined in Eqs. (B.14) and (B.16) vanish in case of symmetry, and that the symmetric version of Eq. (B.22) becomes

$$I_i = \int_{-\bar{y}_4}^{-\bar{y}_3} \frac{y^i f(y)}{\tilde{\Psi}_-(y)} dy + \int_{\bar{y}_3}^{\bar{y}_4} \frac{y^i f(y)}{\tilde{\Psi}_+(y)} dy = \int_{\bar{y}_3}^{\bar{y}_4} \frac{(1 - (-1)^i) y^i f(y)}{\tilde{\Psi}_+(y)} dy, \quad i = 0, 3, \tag{B.85}$$

such that $I_0 = I_2 = 0$. The four conditions (B.23) to (B.26) now reduce to

$$C_0 + D_0 = 0, \tag{B.86}$$

$$D_2 = 0, \tag{B.87}$$

which can also be expressed as

$$C_0 + I_3 = 0, \tag{B.88}$$

$$I_1 = 0. \tag{B.89}$$

Just as in Eqs. (B.33) and (B.34) for the asymmetric case we require the integral of the slip gradient to vanish over each of the slip patches which now leads to a single equation

$$\int_{\bar{y}_3}^{\bar{y}_4} \frac{1}{\tilde{\Psi}_+(y)} \int_{\bar{y}_3}^{\bar{y}_4} \frac{\tilde{\Psi}_+(\xi) 2\xi f(\xi)}{(y^2 - \xi^2)} d\xi dy + \int_{\bar{y}_3}^{\bar{y}_4} \frac{C_0}{\tilde{\Psi}_+(y)} dy = 0, \tag{B.90}$$

from which we can compute C_0 . The three conditions to determine C_0 , I_1 and I_3 are therefore given by Eqs. (B.88) to (B.90).

Alternatively we can start from the four ‘shortcut’ conditions (B.49) to (B.52). Noting that, apart from a sign, the integrals (B.49) and (B.50) are now identical, we obtain

$$\int_{\bar{y}_3}^{\bar{y}_4} \tilde{\Psi}_+(y) \int_{\bar{y}_3}^{\bar{y}_4} \frac{\xi f(\xi)}{\tilde{\Psi}_+(\xi)(y^2 - \xi^2)} d\xi dy = 0 \tag{B.91}$$

as the first of the two required conditions while the other one is identical to Eq. (B.89):

$$\int_{\bar{y}_3}^{\bar{y}_4} \frac{y f(y)}{\tilde{\Psi}_+(y)} dy = 0. \tag{B.92}$$

Fig. B.1 depicts the values of C_0 for the symmetric full formulation (gray solid curves) and the symmetric alternative (short-cut) formulation (orange dashed curves), in addition to the asymmetric results discussed before. It can be seen that the two curves for the symmetric formulation exactly overlap, just like in the asymmetric formulation. Note that there is not much difference between the C_0 values for the symmetric and the asymmetric cases because of the small amount of asymmetry in the example considered.

B.6.3. Double patch merging into a single patch

In this section we show that the symmetric single patch solution can be viewed as a limit case of the symmetric double patch solution. Suppose we have a sequence of double patch solutions (B.84) satisfying conditions (B.91) and (B.92); suppose furthermore that $\bar{y}_3 \rightarrow 0$. In that case we find

$$\lim_{\bar{y}_3 \rightarrow 0} \tilde{\Psi}_\pm(y) = |y| \sqrt{\bar{y}_4^2 - y^2} = |y| \tilde{\Phi}(y), \tag{B.93}$$

which means that the symmetric double-patch solution (B.84) becomes

$$\begin{aligned} \lim_{\bar{y}_3 \rightarrow 0} g(y) &= \frac{|y| \tilde{\Phi}(y)}{\pi^2} \int_0^{\bar{y}_4} \frac{2\xi f(\xi)}{|\xi| \tilde{\Phi}(\xi)} \left(\frac{1}{y^2 - \xi^2} \right) d\xi \\ &= \frac{2y \tilde{\Phi}(y)}{\pi^2} \int_0^{\bar{y}_4} \frac{f(\xi)}{\tilde{\Phi}(\xi)(y^2 - \xi^2)} d\xi, \end{aligned} \tag{B.94}$$

which is the identical to the symmetric single-patch solution (B.79).

Condition (B.91) implies that $G(\bar{y}_3) = G(\bar{y}_4)$, with G indicating the primitive of g , which means that we also have $G(-\bar{y}_4) = G(-\bar{y}_3) = G(\bar{y}_3) = G(\bar{y}_4)$, because $g(y) = 0$ for $-\bar{y}_3 < y < \bar{y}_3$. This means that for $\bar{y}_3 \rightarrow 0$ the symmetric double-patch condition (B.91) also satisfies the symmetric single-patch condition (B.82).

Note that in order to determine \bar{y}_4 for the symmetric single-patch and double-patch solutions respectively, we have different conditions: see Eqs. (B.82) and (B.92). However, just at the point where $\bar{y}_3 = 0$, both conditions become identical:

$$\lim_{\bar{y}_3 \rightarrow 0} \int_{\bar{y}_3}^{\bar{y}_4} \frac{y f(y)}{\tilde{\Psi}_+(y)} dy = \int_0^{\bar{y}_4} \frac{y f(y)}{y \tilde{\Phi}(y)} dy = \int_0^{\bar{y}_4} \frac{f(y)}{\tilde{\Phi}(y)} dy. \tag{B.95}$$

Appendix C. Augmented Gauss-Chebyshev quadrature with analytical inversion

C.1. Formulation

We refer to Mulhopp (1938), Erdogan and Gupta (1972), Erdogan et al. (1973) and Kalandiya (1975) for detailed derivations of the original augmented Gauss–Chebyshev quadrature procedure, and to Hills et al. (1996) and Viesca and Garagash (2018) for further developments and implementation details related to fracture mechanics. The resulting integration formulas can be expressed as

$$\int_{y_-}^{\bar{y}_+} \frac{f(\xi)}{\Phi(\xi)} d\xi \approx \sum_{j=1}^N w_j f(\xi_j) \quad (\text{Gauss–Chebyshev}), \tag{C.1}$$

for regular integrals, and

$$\int_{y_-}^{\bar{y}_+} \frac{f(\xi)}{\Phi(\xi)(y - \xi)} d\xi \approx \sum_{j=1}^N \frac{w_j f(\xi_j)}{y_i - \xi_j} \quad (\text{Augmented Gauss–Chebyshev}), \tag{C.2}$$

for Cauchy-type singular integrals, where

$$\Phi(\xi) = \sqrt{-(\xi - \bar{y}_-)(\xi - \bar{y}_+)}, \tag{C.3}$$

and where we use the scaling

$$y_i = z_i \bar{y} + \bar{y}, \quad \xi_j = \zeta_j \bar{y} + \bar{y}, \tag{C.4}$$

$$\bar{y} = \frac{\bar{y}_- + \bar{y}_+}{2}, \quad \bar{y} = \frac{\bar{y}_+ - \bar{y}_-}{2}. \tag{C.5}$$

with, for augmented first-kind Gauss–Chebyshev quadrature,

$$w_j = \frac{\pi}{N}, \tag{C.6}$$

$$\zeta_j = \cos \frac{\pi(j - \frac{1}{2})}{N}, \quad j = 1, \dots, N, \tag{C.7}$$

$$z_i = \cos \frac{\pi i}{N}, \quad i = 1, \dots, N - 1, \tag{C.8}$$

or, for augmented second-kind Gauss–Chebyshev quadrature,

$$w_j = \frac{\pi(1 - \zeta_j^2)}{N + 1}, \tag{C.9}$$

$$\zeta_j = \cos \frac{\pi j}{N + 1}, \quad j = 1, \dots, N, \tag{C.10}$$

$$z_i = \cos \frac{\pi(i - \frac{1}{2})}{N + 1}, \quad i = 1, \dots, N + 1. \tag{C.11}$$

Eqs. (C.7) and (C.10) are expression for first-kind and second-kind Chebyshev points which are the N zeros of the first-kind and second-kind Chebyshev polynomials $T_N(z)$ and $U_N(z)$ respectively, defined on the domain $-1 < z < 1$. Eqs. (C.8) and (C.11) provide two sets of complementary points which are located mid in-between the corresponding Chebyshev points. Eqs. (C.5) represent the mid point location and the half-length of the integration interval and can be used to rescale from $-1 < z < 1$ to $\bar{y}_- < y < \bar{y}_+$, and from $-1 < \zeta < 1$ to $\bar{y}_- < \xi < \bar{y}_+$, with the aid of Eqs. (C.4). In this formulation the values of y and ξ are both restricted to remain within the integration boundaries \bar{y}_- and \bar{y}_+ where the discrete values y_i are collocation points for which the quadrature is exact if the function $f(\xi)$ is an $(N - 1)$ th degree polynomial (Mason and

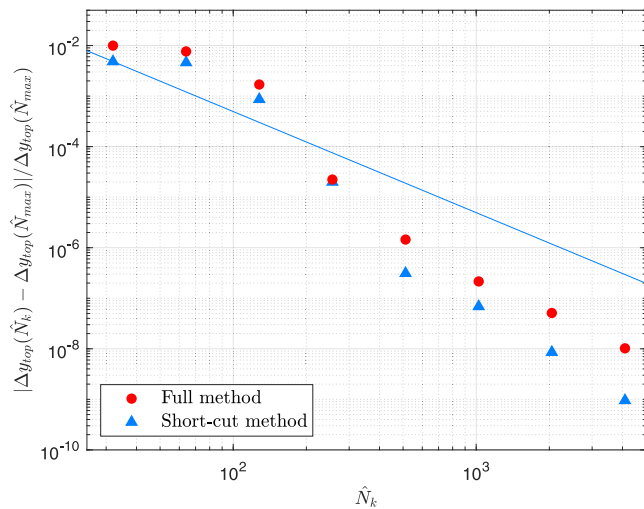


Fig. C.1. Convergence behavior of augmented Chebyshev quadrature as used in the “full” and “short cut” approaches to compute coupled fault slip in the example with parameters from Table 1. The figure displays the relative error in the length of the top slip patch $\Delta y_{top} = \bar{y}_4 - \bar{y}_3$, as a function of the number of Chebyshev points per slip patch $\hat{N}_k = 2^k$, $k = 5, \dots, 12$. The relative errors have been computed with respect to the results for $\hat{N}_{max} = 2^{13} = 8192$ points for each of the methods. The solid blue line indicates algebraic convergence for which the relative error is proportional to $\frac{1}{\hat{N}_k}$.

Handscamb, 2003). This formulation is relevant for Cauchy-type singular integrals, in which case the numerical result should be interpreted as the principal value. The variable y may also take on values outside the integration limits, in which case the integral is no longer singular and y just becomes a parameter. Formulas for integrals with terms that differ from those in Eqs. (C.1) and (C.2) can be derived starting from these equations by moving all non-conforming terms to the function $f(\xi)$.

We note that the original augmented Gauss–Chebyshev formulation, as applied to solve singular integral equations, relies on numerical inversion (though solving a system of equations) as part of the integration procedure to determine the unknown function. In our approach, where we use analytical inversion prior to integration, we only employ the quadrature elements of the original formulation without performing matrix inversion.

C.2. Computational aspects

We implemented our version of the augmented Gauss–Chebyshev quadrature scheme in Matlab. We used the standard function `fsolve` for the iterative computation of the slip patch boundaries \bar{y}_i , $i = 1, \dots, 4$; implemented a predictor–corrector-type variable-stepsize algorithm to progress the change in incremental pressure Δp ; and used Matlab’s vectorization capacities wherever possible.

We used first-kind Gauss–Chebyshev quadrature to integrate expressions with unbounded end-point values, such as Eqs. (B.36) to (B.39), and its second-kind companion to integrate expressions with bounded endpoints, such as Eqs. (B.40) and (B.41). As a result, the solution of both the “full” and the alternative “short-cut” versions of our coupled approach obtain a numerical convergence that is better than algebraic, a feature often referred to as *spectral convergence* (Boyd, 2001; Viesca and Garagash, 2018). We note that in our implementation, in which we use analytical inversion prior to integration, it are the endpoints of the known function that determine the best choice of the Gauss–Chebyshev method, and not the expected endpoints of the unknown function. This is as opposed to the original augmented Gauss–Chebyshev method, which relies on numerical inversion as part of the integration procedure.

Fig. C.1 illustrates the convergence behavior as a function of the number of Chebyshev points per slip patch \hat{N}_k . Algebraic convergence

is indicated with a solid blue line, and spectral convergence can be observed for $\hat{N}_k = 2^8$ up to $\hat{N}_k = 2^{12}$ where the relative error has been computed with respect to the most accurate results for $\hat{N}_k = 2^{13}$. For $\hat{N}_k = 2^5$ to $\hat{N}_k = 2^7$ convergence is less favorable because the results are influenced by the extent to which the Chebyshev points sufficiently cover the pre-slip Coulomb stress peaks around $y = \pm a$. Fig. A.2 (left) in Appendix A illustrates that, for the example considered, a number of $\hat{N}_k = 2^8 = 256$ points per patch gives a reasonable coverage.

Clock times scale approximately quadratically with the number of Chebyshev points \hat{N}_k because of the convolution term in the Cauchy integrals. A better performance may be possible with the use of the fast Fourier transform, but we did not pursue this option in the current paper. As an alternative to augmented Gauss–Chebyshev quadrature we also implemented a variable-support trapezoidal scheme using a nonuniform grid consisting of first-kind or second-kind Chebyshev points. The Gauss–Chebyshev implementation typically performed considerably faster (up to about half the clock time) than the trapezoidal scheme for coupled simulation of fault slip. To give an indication of the computational performance: with 230 variable-sized pressure steps and 256 Chebyshev points per slip patch, it takes a few seconds on a standard laptop to generate the red curves in Fig. 3.

References

- Bilby, B., Eshelby, J., 1968. Dislocations and the theory of fracture. *Fracture - An Advanced Treatise*. Vol. 1, Academic Press, pp. 99–182.
- Biot, M., 1941. General theory of three-dimensional consolidation. *J. Appl. Phys.* 12, 155–164, URL: <http://dx.doi.org/10.1063/1.1712886>.
- Boyd, J., 2001. *Chebyshev and Fourier Spectral Methods*, second ed. Dover.
- Bruhat, L., Segall, P., 2017. Deformation rates in northern Cascadia consistent with slow updip propagation of deep interseismic creep. *Geophys. J. Int.* 211, 427–449, URL: <http://dx.doi.org/10.1093/gji/ggx317>.
- Buijze, A., Van den Bogert, P., Wassing, B., Orlic, B., 2019. Nucleation and arrest of dynamic rupture induced by reservoir depletion. *J. Geophys. Res.: Solid Earth* 124, 3620–3645, URL: <http://dx.doi.org/10.1029/2018JB016941>.
- Buijze, A., Van den Bogert, P., Wassing, B., Orlic, B., Ten Veen, J., 2017. Fault reactivation mechanisms and dynamic rupture modelling of production-induced seismic events in a Rotliegend gas reservoir. *Neth. J. Geosci.* 96, S131–S148, URL: <http://dx.doi.org/10.1017/njg.2017.27>.
- Cornelissen, P., Meulenbroek, B., Jansen, J., 2024. On the derivation of closed-form expressions for displacements, strains and stresses inside poroelastic reservoirs. *J. Geophys. Res.: Solid Earth* 129, e2023JB027733, URL: <http://dx.doi.org/10.1029/2023JB027733>.
- Elsworth, D., Spiers, C., Niemeijer, A., 2016. Understanding induced seismicity. *Science* 354, 1380–1381, URL: <http://dx.doi.org/10.1126/science.aal2584>.
- Erdogan, F., Gupta, G., 1972. On the numerical solution of singular integral equations. *Quart. Appl. Math.* 29, 525–534, URL: <https://www.jstor.org/stable/45340623>.
- Erdogan, F., Gupta, G., Cook, T., 1973. Numerical solution of singular integral equations. *Methods of Analysis and Solutions of Crack problems*. Noordhoff, pp. 368–425.
- Estrada, R., Kanwal, R., 2000. *Singular Integral Equations*. Birkhäuser.
- Fjaer, E., Holt, R., Horsrud, P., Raaen, A., Risnes, R., 2021. *Petroleum Related Rock Mechanics*, third ed. Elsevier.
- Foulger, G., Wilson, M., Gluyas, J., Julian, B., Davies, R., 2018. Global review of human-induced earthquakes. *Earth-Sci. Rev.* 178, 438–514, URL: <http://dx.doi.org/10.1016/j.earscirev.2017.07.008>.
- Garagash, D., Germanovich, L., 2012. Nucleation and arrest of dynamic slip on a pressurized fault. *J. Geophys. Res.* 117, B10310, URL: <http://dx.doi.org/10.1029/2012JB009209>.
- Golberg, M., 1990. *Introduction to the numerical solution of Cauchy singular integral equations*. Numerical Solution of Integral Equations. Plenum Press, pp. 183–308.
- Heimisson, E., Liu, S., Lapusta, N., Rudnicki, J., 2022. A spectral boundary-integral method for faults and fractures in a poroelastic solid: simulations of a rate-and-state fault with dilatancy, compaction, and fluid injection. *J. Geophys. Res.: Solid Earth* 127, e2022JB024185, URL: <http://dx.doi.org/10.1029/2022JB024185>.
- Hergert, T., Haug, C., Henk, A., Nüchter, J., 2022. Modelling production-induced dynamic rupture of intra-graben faults and related earthquakes in the North German Basin. *Geomech. Energy Environ.* 32, 100339, URL: <http://dx.doi.org/10.1016/j.gete.2022.100339>.
- Hills, D., Kelly, P., Dai, D., Korsunsky, A., 1996. *Solution of Crack Problems - the Distributed Dislocation Technique*. Kluwer Academic Publishers.
- Jansen, J., Meulenbroek, B., 2022. Induced aseismic slip and the onset of seismicity in displaced faults. *Neth. J. Geosci.* 101, URL: <http://dx.doi.org/10.1017/njg.2022.9>.
- Jansen, J., Singhal, P., Vossepoel, F., 2019. Insights from closed-form expressions for injection- and production-induced stresses in displaced faults. *J. Geophys. Res.: Solid Earth* 124, 7193–7212, URL: <http://dx.doi.org/10.1029/2019JB017932>.

- Kalandiya, A.I., 1975. *Mathematical methods of two-dimensional elasticity*. Mir Publishers, Moscow.
- Lehner, F., 2019. An Analysis of Depletion-Induced Fault Stressing - New Closed-Form Analytical Solutions. Technical Report, Nederlandse Aardolie Maatschappij, URL: <http://www.nam.nl/feiten-en-cijfers/onderzoeksrapporten.html>.
- Lewin, L., 1968. The solution of singular integral equations over a multiple interval and applications to multiple diaphragms in rectangular waveguide. *SIAM J. Appl. Math.* 16, 417–438, URL: <https://www.jstor.org/stable/2099304>.
- Mason, J., Handscomb, D., 2003. *Chebyshev Polynomials*. Chapman and Hall.
- Mavko, G.M., 1982. Easy computation of static stress drop, slip, and moment on two-dimensional heterogeneous faults. *Bull. Seismol. Soc. Am.* 72, 1499–1508, URL: <http://dx.doi.org/10.1785/BSSA0720051499>.
- Mulders, F., 2003. Modelling of Stress Development and Fault Slip in and Around a Producing Gas Reservoir (Ph.D. thesis). Delft University of Technology, URL: <http://resolver.tudelft.nl/uuid:be742135-10d7-4d69-bdee-f808b5926065>.
- Multhopp, H., 1938. Die Berechnung der Auftriebsverteilung von Tragflügeln. *Luftfahrtforschung* 15 (4), 153–166.
- Muntendam-Bos, A., Hoedeman, G., Polychronopoulou, K., Draganov, D., Weemstra, C., Van der Zee, W., Bakker, R., Roest, H., 2022. An overview of induced seismicity in the Netherlands. *Neth. J. Geosci.* 101, URL: <http://dx.doi.org/10.1017/njg.2021.14>.
- Muskhelishvili, N., 1953. *Singular Integral Equations*. Wolters-Noordhoff, Groningen.
- Novikov, A., Shokrollahzadeh Behbahani, S., Voskov, D., Hajibeygi, H., Jansen, J., 2023. Benchmarking analytical and numerical simulation of induced fault slip. In: 57th US Rock Mechanics/Geomechanics Symposium. URL: <http://dx.doi.org/10.56952/ARMA-2023-0695>. [paper ARMA 23-695. 25–28 June, Atlanta, USA].
- Novikov, A., Voskov, D., Khait, M., Hajibeygi, H., Jansen, J., 2022. A scalable collocated finite volume scheme for simulation of induced fault slip. *J. Comput. Phys.* 469, 111598, URL: <http://dx.doi.org/10.1016/j.jcp.2022.111598>.
- Ohnaka, M., 2013. *The Physics of Rock Failure and Earthquakes*. Cambridge University Press.
- Pogorzelski, W., 1966. *Integral Equations and their Applications*. Pergamon Press.
- Rice, J., 1968. *Mathematical analysis in the mathematics of fracture. Fracture - An Advanced Treatise*. Vol. 2, Academic Press, pp. 191–311.
- Rice, J., 1980. *The mechanics of earthquake rupture. Physics of the Earth's Interior*. Italian Physical Society / North Holland Publ. Co., pp. 555–649.
- Roest, J., Kuilman, W., 1994. Geomechanical analysis of small earthquakes at the Eleveld gas reservoir. In: SPE-ISRM Rock Mechanics in Petroleum Engineering Conference. URL: <http://dx.doi.org/10.2118/28097-MS>. [paper SPE 28097. 29-31 Aug., Delft, The Netherlands].
- Roest, J., Mulders, F., 2000. Overview modelling gas production-induced seismicity mechanisms. In: Eurock 2000 Symposium. URL: <http://resolver.tudelft.nl/uuid:6913b331-83f4-499a-822a-6d2af5091580>. [27–31 March, Aachen, Germany].
- Rudnicki, J., 2002. Elshelby transformations, pore pressure and fluid mass changes, and subsidence. In: *Poromechanics II, 2nd Biot Conf. Poromech. Aug. 26-28, Grenoble, France*.
- Rudnicki, J., 2011. Eshelby's technique for analyzing inhomogeneities in geomechanics. *Mechanics of Crustal Rocks*. Springer, Vienna, pp. 43–72.
- Scholz, C., 2019. *The Mechanics of Earthquakes and Faulting*, third ed. Cambridge.
- Segall, P., 1985. Stress and subsidence resulting from subsurface fluid withdrawal in the epicentral region of the 1983 Coalinga earthquake. *J. Geophys. Res.* 90, 6801–6816, URL: <http://dx.doi.org/10.1029/JB090iB08p06801>.
- Segall, P., 1989. Earthquakes triggered by fluid extraction. *Geology* 17, 942–946, URL: [http://dx.doi.org/10.1130/0091-7613\(1989\)017<0942:ETBFE>2.3.CO;2](http://dx.doi.org/10.1130/0091-7613(1989)017<0942:ETBFE>2.3.CO;2).
- Segall, P., 2010. *Earthquake and Volcano Deformation*. Princeton University Press.
- Suckale, J., 2009. *Induced Seismicity in Hydrocarbon Fields*. Vol. 51, Academic Press, pp. 55–106.
- Uenishi, K., Rice, J., 2003. Universal nucleation length for slip-weakening rupture instability under nonuniform loading. *J. Geophys. Res.: Solid Earth* 108, 2042, URL: <http://dx.doi.org/10.1029/2001JB001681>.
- Van den Bogert, P., 2015. Impact of various modelling options on the onset of fault slip and fault slip response using 2-dimensional finite-element modelling. URL: <https://www.nam.nl/feiten-en-cijfers/onderzoeksrapporten.html>.
- Van den Bogert, P., 2018. Depletion-induced fault slip and seismic rupture: 2D geomechanical models for the Groningen field, The Netherlands. URL: <https://www.nam.nl/feiten-en-cijfers/onderzoeksrapporten.html>.
- Van Wees, J., Fokker, P., Van Thienen-Visser, K., Wassing, B., Osinga, S., Orlic, B., Ghouri, S., Buijze, L., Pluymaekers, M., 2017. Geomechanical models for induced seismicity in The Netherlands: inferences from simplified analytical, finite element and rupture model approaches. *Neth. J. Geosci.* 96, S183–S202, URL: <http://dx.doi.org/10.1017/njg.2017.38>.
- Van Wees, J., Pluymaekers, M., Osinga, S., Fokker, P., Van Thienen-Visser, K., Orlic, B., Wassing, B., Hegen, D., Candela, T., 2019. 3-d mechanical analysis of complex reservoirs: a novel mesh-free approach. *Geophys. J. Int.* 219, 1118–1130, URL: <http://dx.doi.org/10.1093/gji/ggz352>.
- Viesca, R., Garagash, D., 2018. Numerical methods for coupled fracture problems. *J. Mech. Phys. Solids* 113, 13–34, URL: <http://dx.doi.org/10.1016/j.jmps.2018.01.008>.
- Viesca, R., Rice, J., 2012. Nucleation of slip-weakening rupture instability in landslides by localized increase of pore pressure. *J. Geophys. Res.: Solid Earth* 117, B03104, URL: <http://dx.doi.org/10.1029/2011JB008866>.
- Wang, H., 2000. *Theory of Linear Poroelasticity with Applications to Geomechanics and Hydrogeology*. Princeton University Press.
- Weertman, J., 1996. *Dislocation Based Fracture Mechanics*. World Scientific.
- Wu, H., Vilarrasa, V., De Simone, S., Saaltink, M., Parisio, F., 2021. Analytical solution to assess the induced seismicity potential of faults in pressurized and depleted reservoirs. *J. Geophys. Res.: Solid Earth* 126, e2020JB020436, URL: <http://dx.doi.org/10.1029/2020JB020436>.